4. Beam-beam interactions

Presently, as it was shown in the previews section, the observed luminosity evolution is mainly driven by basic diffusion mechanisms; and the beam-beam effects produce comparatively little effect during the store. Nevertheless they cause significant particle loss during the beam injection, acceleration and squeeze. Presently, the beam-beam effects represent the most fundamental limitation of the peak luminosity of the collider. If not addressed their effect will be even more detrimental at the final Run II parameters.

Beam-beam phenomena are well known to have an effect on the antiproton beam circulating the Tevatron collider, but there is evidence that they play some roll on the proton beam as well. Presently, proton intensity is about ten times larger than the antiproton intensity; therefore the beam-beam effects have largely acted on the antiprotons. The effects of the antiprotons on the protons have until now been relatively benign but that may change at higher antiproton currents.

In this section we will consider how the beam-beam interaction affect the beam dynamics on the different stages of collider operation: injection, acceleration and squeeze. Although there are a lot of commonalities, there are also phenomena, which make them different.

4.1. Present operating scenario

The collider shot starts with downloading 36 proton bunches to the collider central orbit. Every proton bunch is downloaded separately (see Figure 1). After all proton bunches are downloaded the injection helix is opened and, then, antiprotons are injected four bunches at a time to the antiproton helical orbit. Typically it takes about 15-20 minutes to transfer all antiproton bunches to their injection helix. Because of beam-beam effects, and dynamic and physical aperture limitations the lifetime of both beams is severely affected and the beams loose up to 10% of their intensity in the course of injection.

After all bunches are injected, acceleration to top energy takes about 85 seconds. Then, the interaction regions optics (IRs) is changed to lower β^* from 1.6 m to 0.35 m at B0 and D0. This process typically takes about 2 minutes. Finally the beams are brought into collision by collapsing the separation bumps around the IPs. During a high energy physics store each bunch experiences two head-on collisions with bunches in the opposing beam and seventy long-range interactions. At all other stages of the operational cycle, each bunch experiences only long-range interactions – seventy two in all. Performance limitations from beam-beam effects until now have been primarily due to these long-range interactions.

At injection the beam lifetime at the central orbit is a few hundred hours. However it is drastically reduced after helix is opened (Fig.1). The antiproton lifetime is in the range of 1-10 hors and is mainly determined by the beam-beam effects. In the beam studies with only antiprotons injected into pbar helix, the lifetimes were found to be in the range of 20 hrs. By contrast, the proton lifetime at the proton helix is determined by particle loss due to dynamic and physical aperture limitations and is strongly affected by machine chromaticity due to dynamic aperture reduction for particle with large synchrotron

amplitudes. Presence of antiprotons does not produce any significant affect on the proton lifetime.

The largest antiproton losses before collision are initiated are observed during acceleration when about 10-15% of the beam is lost. Without protons, the losses during acceleration are much smaller - about 2%. Proton losses during acceleration are about 5% (with well coalesced bunches) and do not change much when antiprotons are not present. During the squeeze, losses in both beams have been low since the helix was changed to increase the separation at sequence 13 of the squeeze in July 2002.

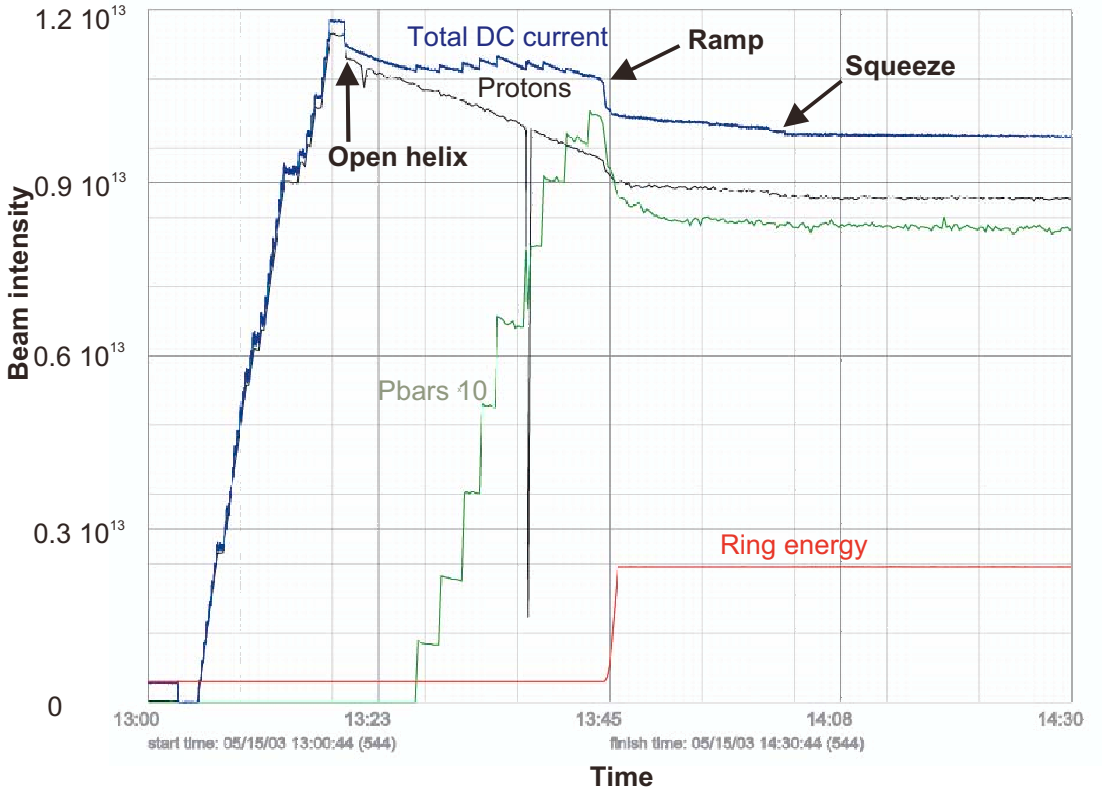

Figure 1. Dependence of proton and antiproton beam intensities on time during collider shot for Store 2549 (May 15, 2003). Upper line – total DC current in the ring; center line – proton beam current, lower line – antiproton beam current increased in 10 times .

Table 1. Typical beam parameters and particle loss observed during Run II

	03/02	10/02	01/03	03/03
Protons/bunch at low-beta, 10^{11}	1.4	1.70	1.8	2.05
Pbars/bunch at low-beta, 10^{11}	0.075	0.22	0.20	0.23
P-loss at 150 GeV	23%	14%	16%	10%
Pbar-loss at 150 GeV	20%	9%	4%	4%
P-loss on ramp	7%	6%	9%	5%
Pbar-loss on ramp	14%	8%	12%	11%
Pbar-loss in squeeze	25%	5%	3%	2%
Initial pbar emitt. growth rate $\varepsilon_x/\varepsilon_y$ [% /hr]	-	0/0.8	1/2.4	0.4/1.2
Initial proton emitt. growth rate $\varepsilon_x/\varepsilon_y$ [% /hr]	-	3.4/2.4	2.4/2.4	2/1.2

Table 1 presents average particle loss at different stages of collider shot since March 2002. In spite of growing proton intensity the antiproton losses have decreased during the last year mostly due to improvements of helical beam separation and better control of the orbits, tunes and chromaticities. Antiproton and proton losses on the ramp together with proton losses at 150 GeV are the dominant contributors to the Tevatron inefficiency.

Table 2. Collider parameters

	Injection	Collision
Ring circumference, C [m]	6283.19	
Beam momentum, P_0 [GeV/c]	149.7	980
Bare lattice proton betatron tunes, ν_x/ν_y	20.585/20.575	20.580/20.570
Bare lattice pbar betatron tunes, ν_x/ν_y	20.585/20.575	20.570/20.580
Momentum compaction, α_M	0.00283	
Harmonic number, q	1113	
RF frequency, f_{RF} [MHz]	53.104	53.105
RF voltage, V_0 [MV/turn]	1.0	1.0
Small amplitude synchrotron frequency, f_s [Hz]	86.5	34.8
Synchrotron tune, ν_s	0.00181	0.000723
Bucket size, [eV s]	4.27	10.8
Bucket height, $\Delta p/p_{max}$, 10^{-3}	1.17	0.456

The emittance growth of antiprotons have been larger vertically than horizontally and, as will be shown below, is attributed to the beam-beam interactions. Proton emittance growth rates are mainly due to intra-beam scattering - the growth rates in the transverse planes are nearly equalized due to strong coupling.

Table 2 shows major collider parameters. The helical beam separation is different at different steps of the collider cycle since the requirements are different (see Section 5 for detail) Table 3 presents voltages on the high voltage separators, which are presently used at the injection and collisions; and Figure 2 depicts corresponding relative beam separations for all collision points at the collision cogging. If it is not pointed out otherwise these parameters and beam separations are used below. The relative beam separation presented in Figure 2 are computed using the following equation:

Table 3. Voltages of high voltage separators used for collider operation in May 2003

	Injection	Collision
A17V	0	±6.90
A49V	0	±83.5
A49H	0	±100.
B11V	±22.62	±100.
B11H	±36.99	±100.
B17H	±64.35	±47.7
C17V	±58.85	±48.4
C49V	0	±83.0
C49H	0	±93.0
D11V	0	±100.
D11H	0	±86.8
D48H	0	±15.1

$$S = \sqrt{\left(d_x / \sigma_x^{(\beta)}\right)^2 + \left(d_y / \sigma_y^{(\beta)}\right)^2} \quad , \qquad (1)$$

where d_x and d_y are the total horizontal and vertical beam separations, and $\sigma_x^{(\beta)}$ and $\sigma_y^{(\beta)}$ are the rms betatron beam sizes.

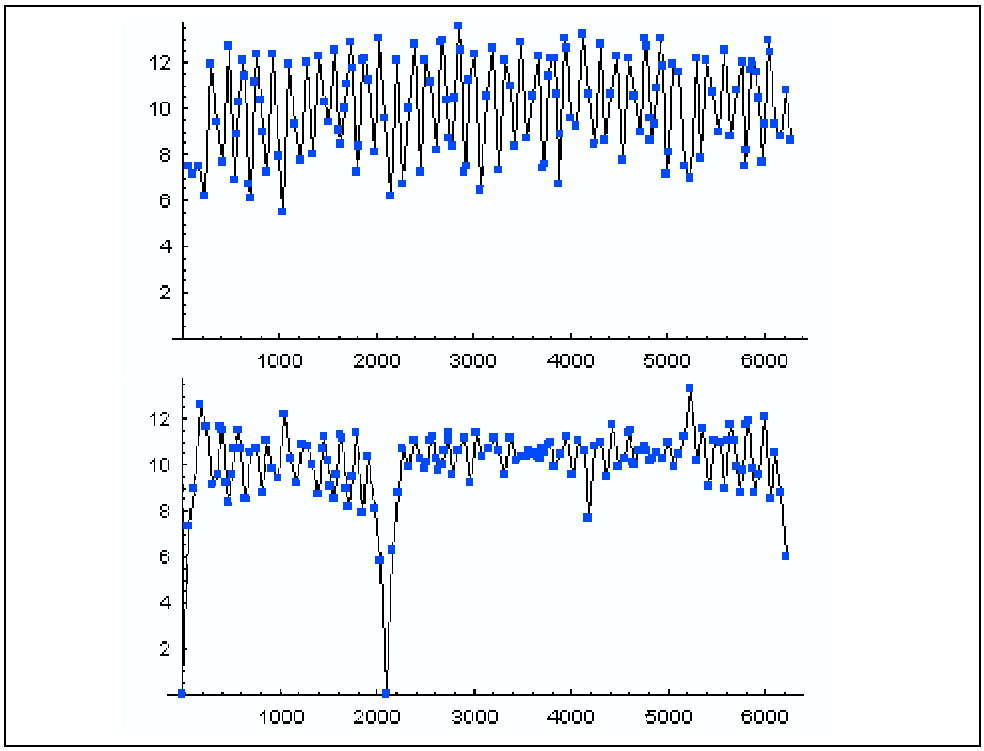

Figure 2. Relative beam separation starting from B0 for injection (top) and collision helices with voltages presented in Table 3. Reference emittance 20 mm mrad.

4.2. Incoherent beam-beam effects

By ***incoherent*** effects we understand the effects produced by the quasi-equilibrium field of the opposing beam, in contradistinction to the ***coherent*** beam-beam effect which results in correlated oscillations in both beams (see next section).

Particle motion in the field of the opposing beam is governed by the Hamiltonian which in the case of short bunches ($\sigma_s << \beta^*$) with Gaussian charge distribution can be presented in the form (see Refs.[1,2])

$$H_{bb} = -\frac{2r_p N}{\gamma} \ddot{a}_p(\theta - \theta_{IP}) \int_0^1 \frac{dt}{t\sqrt{1+(r^2-1)t^2}} \times \exp\left\{ -\frac{(d_x + \tilde{x} + D_x\delta_p + \alpha\tilde{z})^2}{2\sigma_x^2} t^2 - \frac{(d_y + \tilde{y})^2}{2\sigma_y^2[1+(r^2-1)t^2]} r^2 t^2 \right\} \tag{2}$$

where $r = \sigma_y/\sigma_x$, is the aspect ratio, $\sigma_{x,y}$ are full (including the synchrotron part) r.m.s. sizes of the opposing beam, α is crossing half-angle (presently $\alpha = 0$), $\tilde{x}, \tilde{y}, \tilde{z}$ are the particle excursions in the course of betatron and synchrotron oscillations, $\delta_p(\theta)$ is the periodic δ-function of the generalized azimuth θ which should not be confused with the momentum deviation δ_p.

Effect of finite bunch length in practically important cases can be taken into account with additional factor (see subsection 4.2.2).

The incoherent beam-beam effects can be classified as the ones affecting the single-particle tunes (amplitude-dependent shifts in tunes, chromaticity and coupling) and the resonances leading to growth (variation in general) in the oscillation amplitudes.

To analyze these effects it is convenient to introduce the action-angle variables I_u, ψ_u, $u = x, y, z$, via relations

$$\tilde{u} = \sqrt{2\beta_u I_u}\cos[\mu_u(\theta) + \psi_u], \quad u = x, y,$$
$$\tilde{z} = \sqrt{2\frac{R\alpha_M}{\nu_s} I_s}\cos(\nu_s\theta - \psi_s), \quad \delta_p = -\sqrt{2\frac{\nu_s}{R\alpha_M} I_s}\sin(\nu_s\theta - \psi_s), \tag{3}$$

where $\mu_{x,y}$ are the betatron phase advances.

4.2.1. Linear and non-linear shifts in tunes, chromaticity and coupling

To obtain the tuneshifts from the Hamiltonian (2) one should average it over θ and all phase angles ψ_u and take derivatives,

$$\Delta\nu_u^{(bb)} = \frac{\partial}{\partial I_u}\langle H_{bb}\rangle, \quad u = x, y, s, \tag{4}$$

Efficient algorithms for calculation of the tuneshifts as functions of all three action variables or just of two transverse ones were presented correspondingly in Refs.[1-3] and [4].

In what follows we will repeatedly cite ***linear*** (i.e. small-amplitude) tuneshifts, which are important from the point of view of the ***bunch-to-bunch tunespread*** arising from a

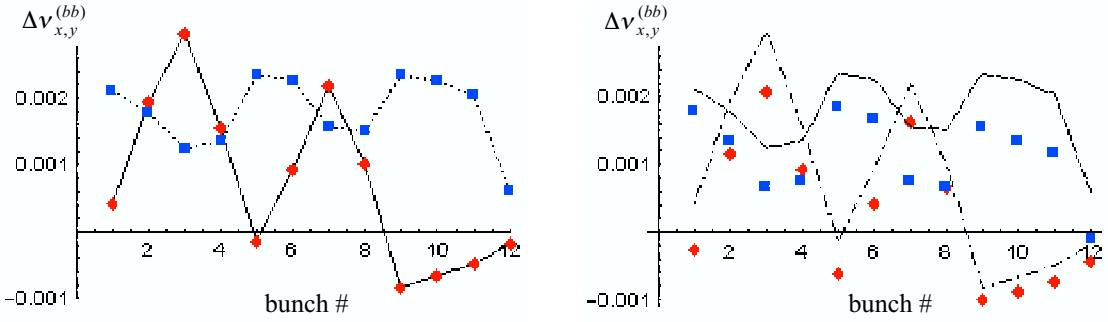

Figure 3. Antiproton bunch-by-bunch linear tuneshifts at 150 GeV with N_p=3·10^{11}; left - analytical calculations (diamonds – horizontal, squares – vertical); right - MAD TWISS command without coupling (diamonds and squares) with bare lattice tunes on the pbar helix 20.5820, 20.5705; lines show analytical values from the left.

different collision schedule for each bunch in a train.

Nonlinear beam-beam effect results in an ***intra-bunch tunespread***. Both tunespreads contribute to the area occupied by the beam in the tune plane and should be reduced in order to avoid dangerous resonances. However, some spreads should remain in order to stabilize coherent instabilities and provide detuning with amplitude from incoherent high-order resonances which are difficult to avoid.

Tuneshifts due to head-on collisions of round beams are well studied, at small amplitudes they are given by the so-called beam-beam parameter

$$\xi = \frac{r_p N_p}{4\pi\gamma\varepsilon_{\perp p}} \tag{5}$$

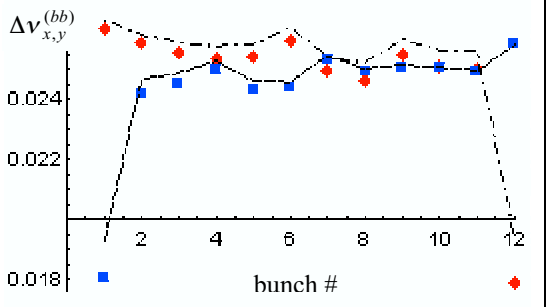

Figure 4. Antiproton bunch-by-bunch linear tuneshifts at collision with N_p=2.7·10^{11} computed with MAD (diamonds – horizontal, squares – vertical) and by analytical formulas (lines)

Linear tuneshifts due to long-range collisions at large separation are given by formulas

$$\Delta\nu_{x,y}^{(bb)} = \mp\frac{r_p N\beta_{x,y}}{2\pi\gamma d^2}\cos 2\phi, \qquad d = \sqrt{d_x^2 + d_y^2}, \quad \phi = \arctan(d_y / d_x). \tag{6}$$

which shows that at a diagonal separation ($|\phi| = \pi/4$) linear tuneshifts vanish.

Figure 3 presents bunch-by-bunch linear tuneshifts at 150 GeV calculated by analytical formulas of Refs.[1,2] (left) and with MAD TWISS command (right) for bare lattice tunes on the pbar helix 20.5820, 20.5705 (feeddown effect from sextupoles not compensated in these calculations). The MAD values occurred much lower than analytical prediction, the reason being strong dynamic beta effect not included in analytical calculations.

The bunch-by-bunch linear tuneshifts at collision are shown in Fig.4; the dynamic beta effect being noticeably weaker except for the so-called PACMAN bunches.

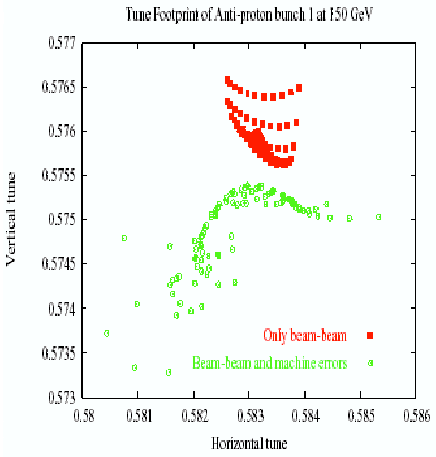

Figure 5. Tune footprint of bunch #1 at injection (to 6σ in each plane) with only beam-beam and with both beam-beam and machine nonlinearities.

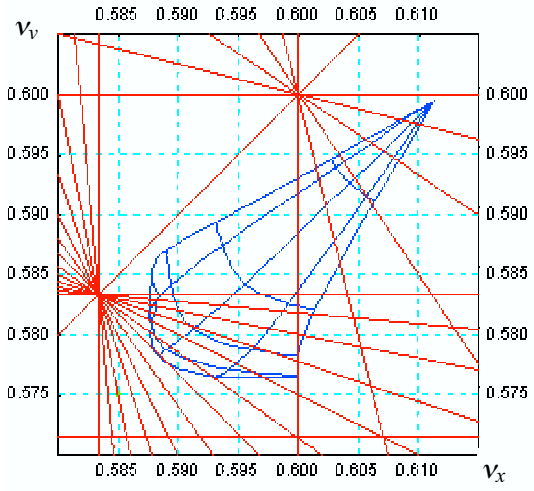

Figure 6. Footprint of bunch #6 at collision with N_p=2.7·10^{11} and the 'standard' WP (green dot); the arc lines are drawn with step 2σ in the transverse amplitude for the reference emittance 15π mm·mrad.

The tuneshifts in the PACMAN bunches (vertical in the first bunch and horizontal in the last) are significantly smaller than in the regular bunches since the PACMAN bunches suffer near-miss interactions only on one side of the nominal IPs at B0 and D0 (see Fig.2, bottom).

Such large difference in the linear tuneshifts makes it difficult to accommodate all bunches in a resonance-free region in the tunes plane; a number of solutions were proposed to reduce the spread in linear tunes: beam-beam compensation with electron lenses and/or pulsed wires; augmenting each proton train by forerunning and trailing bunches. These options are discussed in the corresponding sections of this report.

The tunespread inside each bunch is determined by combination of the beam-beam and machine nonlinearities. As Fig.5 demonstrates at injection the machine nonlinearities dominate.

At collision, on the contrary, the intra-bunch tunespread is almost completely determined by the beam-beam interactions. Fig.6 shows pbar bunch #6 footprint in the tune diagram with bare lattice tunes 20.585, 20.575 ('standard' WP) at the design proton intensity. Red lines show resonances of 5th, 7th and 12th orders. It is obvious that it is impossible to accommodate all particles with amplitudes within 6σ in the area free of these resonances.

4.2.1.1. Beam-beam chromaticity

Due to the finite dispersion at parasitic IPs there should be some dependence of the beam-beam tuneshifts on the synchrotron motion. Calculations show that for the average values of the tuneshifts over the synchrotron period this dependence is negligible.

However, there can be significant variation of the instant values of the tuneshifts which we will treat in terms of the beam-beam contribution to chromaticity.

In the course of synchrotron oscillations the distance between the particle and the center of the opposing bunch varies as $d_{x,y} = d_{x,y0} + D_{x,y}\,\delta_p$ leading to variation of the long-range tuneshift. The corresponding contribution to chromaticity is:

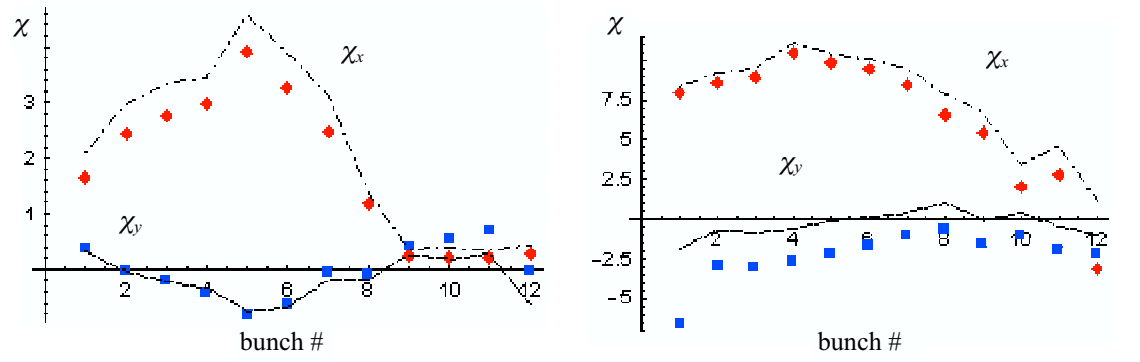

Figure 7. Antiproton bunch-by-bunch linear shifts in chromaticity at injection (left) and collision (right) computed with MAD (diamonds and squares) and by analytical formulas of Ref.[1] (lines)

$$\chi_u \equiv \frac{\partial}{\partial \delta_p}\Delta\nu_u^{(bb)} = D_x \frac{\partial}{\partial d_x}\Delta\nu_u^{(bb)} + D_y \frac{\partial}{\partial d_y}\Delta\nu_u^{(bb)}, \quad u = x, y\,. \tag{7}$$

In the case of large separation we get from eq.(7) an approximation for *linear* (i.e. small betatron amplitude) beam-beam chromaticity:

$$\chi_{x,y} = \pm\frac{r_p N_p \beta_{x,y}}{\pi\gamma d_0^3}[D_x \cos\phi\,(2\cos 2\phi - 1) + D_y \sin\phi\,(2\cos 2\phi + 1)]\,. \tag{8}$$

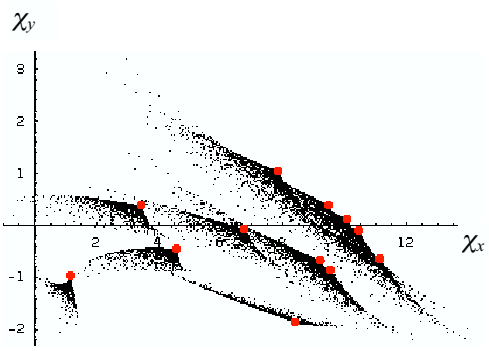

Figure 8. Total $\bar{p}$ distribution in the chromaticity plane at collision, particles with zero betatron amplitudes in each of the 12 bunches in a train are shown with red circles.

In absence of vertical dispersion the chromaticity would vanish if the separation is either vertical or at ϕ = 30°. In practice this requirement cannot be fulfilled.

Figure 7 presents bunch-by-bunch linear beam-beam chromaticity computed with MAD and by analytical formulas of Ref.[2] at injection (N_p=3·10^{11}) and collision (N_p=2.7·10^{11}). In the horizontal plane the beam-beam contribution is comparable with the bare lattice chromaticity (+8 at injection and +16 at collision).

An important feature of the beam-beam chromaticity is its strong dependence on the betatron amplitudes as shown in Fig.8.

Due to large bunch-to-bunch and intra-bunch spreads the chromaticities cannot be made small simultaneously for all particles in all bunches with the help of correction sextupoles.

4.2.1.2. Beam-beam contribution to coupling

Beam-beam interaction may affect the tunes also via its contribution to the cross-plane coupling. The linear effect is described by the terms in the Hamiltonian with the resonance numbers m_x = 1, m_y = ±1 (see next subsection). With the tunes close to the main diagonal, only the term responsible for the difference resonance can be retained, the

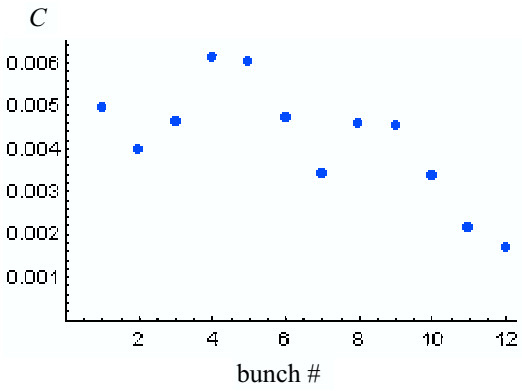

Figure 9. Antiproton bunch-by-bunch linear coupling coefficient at injection computed by analytical formula.

expression for the minimum tunesplit being:

$$C = \left|R_{1,-1}\right| / \sqrt{I_x I_y} \qquad (9)$$

Again, it is instructive to obtain an approximation for large separation (see.eq.(18))

$$C = \frac{r_p N_p \sqrt{\beta_x \beta_y}}{\pi \gamma d_0^2} \left|\sin 2\phi\right| \qquad (10)$$

which shows that linear coupling vanishes when the separation angle is 45°.

The bunch-by-bunch coupling coefficient at injection computed by exact formulas is shown in Fig.9. It is large enough to affect the tunes in some bunches. At collision the beam-beam contribution to coupling is much smaller.

4.2.2. Resonance driving terms and resonance widths

Let us remind the possible effects of incoherent resonances on particle dynamics.

In the vicinity of an isolated resonance

$$\Delta_{\underline{m}} = \underline{m}\cdot\underline{\nu} - n \equiv m_x\nu_x + m_y\nu_y + m_s\nu_s - n \approx 0, \qquad (11)$$

where tunes $\nu_{x,y}$ are assumed to be functions of the action variables, we can drop insignificant terms and going into the rotating frame write the Hamiltonian in the form [5]

$$H \approx \int^{I_1} \Delta_{\underline{m}}(I_1', I_2)\, dI_1' + L_{\underline{m},m_s}(I_s) R_{\underline{m}}(I_1, I_2)\cos\psi_1, \qquad (12)$$

where $R_{\underline{m}}$ is the resonance driving term (RDT), $\psi_1 = m_x\psi_x + m_y\psi_y - m_s\psi_s - n\theta$, $I_1 = (m_x I_x + m_y I_y)/(m_x^2 + m_y^2)$, $I_2 = (m_y I_x - m_x I_y)/(m_x^2 + m_y^2)$ = inv, $L_{\underline{m},ms}(I_s)$ describes the effect of modulation of betatron tunes and/or betatron phase advance at the actual collision point by the synchrotron motion; $L_{\underline{m},ms}(0) = 1$ (let us note that such factorization is not possible in the cases of finite dispersion and/or crossing angle). In all practical cases the synchrotron amplitude itself may be regarded as a constant of motion.

In the case of dominant effect of chromaticity the longitudinal factor is given by the well-known formula (see e.g. Ref.[5])

$$L_{\underline{m},m_s} = \mathrm{J}_{m_s}\left(\frac{m_x\nu_x' + m_y\nu_y'}{\nu_s}\delta_{p0}\right), \qquad (13)$$

where $\delta_{p0} = \sqrt{2R\alpha_M I_s/\nu_s}$ is the synchrotron amplitude, $\mathrm{J}_m(x)$ is the Bessel function of order m.

♦ In the presence of strong nonlinear detuning with amplitude an isolated resonance manifests itself as beatings in the betatron amplitudes, phase space trajectories are bounded forming so-called resonance islands (see Fig.10 for example).

Neglecting variation of $R_{\underline{m}}$ and $\Delta'_{\underline{m}} = \partial\Delta_{\underline{m}}/\partial I_1$ in the vicinity of the fixed point the resonance half-width in the action variable space can be estimated as ($L_{\underline{m},ms} = 1$):

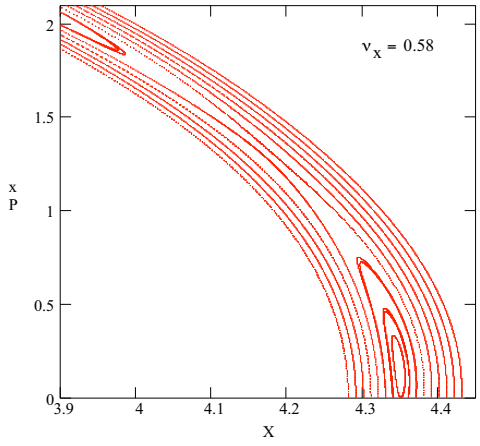

Figure 10. Phase space trajectories on the single-dimensional 12th order resonance $12\nu_x=7$; σ_s=50 cm, $\Delta p/p$=0, two Tevatron IPs with ξ=0.01 each, no long-range collisions, small amplitude island tune is about 0.00023.

$$\delta I_1 \approx 2\left|R_{\underline{m}}/\Delta'_{\underline{m}}\right|^{1/2}, \qquad \delta I_x = m_x \delta I_1, \quad \delta I_y = m_y \delta I_1, \tag{14}$$

In the tunes plane the resonance half-width is given by

$$\delta\Delta_{\underline{m}} \approx 2\left|R_{\underline{m}} \cdot \Delta'_{\underline{m}}\right|^{1/2}. \tag{15}$$

There is a closely related value, *the island tune*, which is the tune of small amplitude libration w.r.t. the stable fixed point in the rotating frame:

$$\nu_{\text{isl}} \approx \left|R_{\underline{m}} \cdot \Delta'_{\underline{m}}\right|^{1/2}. \tag{16}$$

The island tune gives the time scale of particle transport on a resonance.

♦ A group of resonances can create dynamic chaos leading to particle diffusion to large amplitudes if the (refined) Chirikov overlap criterion is satisfied (see e.g. Ref.[6]), i.e. *if the distance between the resonances is less than 3/2 of the sum of the resonance islands half-widths.*

In a real system subject to external noise diffusion will take place anyway, but on a different time scale (see section 4.2.5 for discussion)

♦ Slow variation in the betatron tunes, $\delta\nu_{x,y}$ (which may be called forth by the orbit deviations inside the sextupoles, current ripple in the quadrupoles etc. with spectrum below ν_{isl}) makes the resonance islands move in- and outwards in the phase space transporting the trapped particles to larger amplitudes. This process, which we will call "sweeping", increases the effective width of the resonance as

$$\delta\Delta^{\text{eff}}_{\underline{m}} \approx \delta\Delta_{\underline{m}} + \underline{m} \cdot \underline{\delta\nu} \tag{17}$$

In the case $\nu_s \le \nu_{\text{isl}}$ formula (17) is approximately valid for chromatic tune modulation as well if we put $\underline{\delta\nu} = (\nu'_x \delta_{p0}, \nu'_y \delta_{p0})$.

4.2.3. Beam-beam resonances at collision

With the standard for Tevatron choice of the bare lattice tunes ν_x = 20.585, ν_y = 20.575 the pbar footprint in collision encompasses 5th and 12th order resonances and is quite close to the 7th order resonances (Fig.6).

4.2.3.1. Long-range interaction

In absence of large offsets at the nominal IPs the odd-order resonances are driven by long-range interactions (each bunch in Tevatron experiences 2 head-on and 70 parasitic long-range interactions, there is total of 136 parasitic interaction points).

Let us start with a simple asymptotics for the resonance driving terms at large separations and small betatron amplitudes:

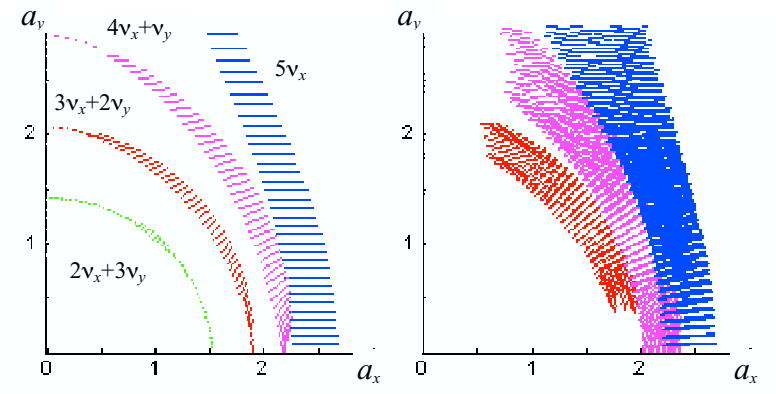

Figure 11. Swing of the normalized transverse amplitudes in pbar bunch#6 at collision on the 5th order resonances and their synchrotron satellites at synchrotron amplitude $\delta_{p0} = 0$ (left) and $\delta_{p0} = 1.25\cdot10^{-4}$ (right). The 'standard' WP, the bare lattice chromaticities put to zero, reference emittance 15π mm·mrad.

$$|R_{\underline{m}}| = \frac{r_p N}{\pi\gamma d_0^p}\frac{(p-1)!}{2^{p/2-1}|m_x|!|m_y|!}(\beta_x I_x)^{\frac{|m_x|}{2}}(\beta_y I_y)^{\frac{|m_y|}{2}}\left|\cos\left(\frac{\pi}{2}m_y + p\phi\right)\right|, \quad (18)$$

where $p = |m_x| + |m_y|$ is the order of the resonance, showing that there are $2p$ values of the angle at which RDT vanishes. However, at separations smaller than 5σ approximation (18) fails. Also, one should use exact formulas of Refs.[1, 2] at the amplitudes commensurable with the separation.

The effect of the 5th order resonances and their synchrotron satellites was studied in Ref.[2]. The betatron tune modulation by synchrotron oscillations turned out to be the strongest mechanism of the satellites excitation; it was shown that the long-range beam-beam interaction itself introduces large chromaticity ($\nu'_{x,y}$~10) sufficient to drive high order satellites.

The resonance widths were calculated using exact formulas which take into account the real dependence of tunes and resonance driving terms on betatron amplitudes. The results are presented in Fig.11 for on-momentum particles in pbar bunch #6 (left plot) when no satellite is excited and for $\delta_{p0} = 1.25\cdot10^{-4}$ (right plot). The bare lattice

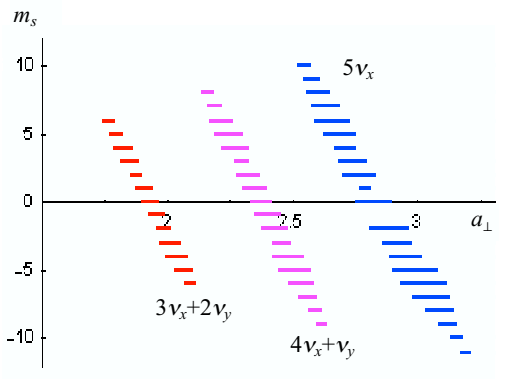

Figure 12. Swing of the transverse amplitude due to individual synchrotron satellites of the 5th order resonances at $\delta_{p0} = 1.25\cdot10^{-4}$.

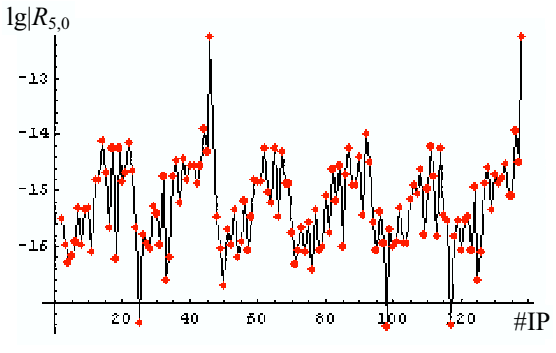

Figure 13. Contribution from all parasitic IPs to the $5\nu_x$ resonance driving term at $a_x = 3$ starting from B0 (nominal IP#1).

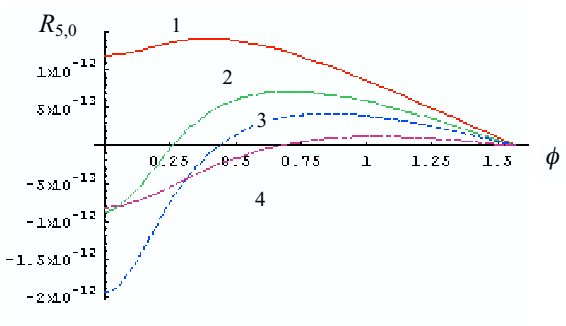

Figure 14. Contribution to $5\nu_x$ RDT from IP#46 vs separation angle at total separation values: 1 – 1.25mm; 2 – 1.5mm, 3 – 1.75mm, 4 – 2.5mm.

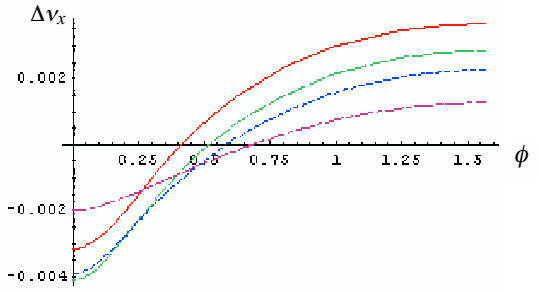

Figure 15. Contribution to $\Delta\nu_x$ from IP#46 vs separation angle at the same values of the total separation as in Fig.14.

chromaticity was set to zero.

In the case of synchrotron oscillations the principal resonances (m_s = 0) are, in accordance with eq.(13), noticeably suppressed (e.g. the $2\nu_x+3\nu_y$ resonance width falls below the chosen threshold, $\Delta a<10^{-3}$). However, due to excitation of numerous satellites the effective resonance width is substantially increased. The satellites overlap is illustrated by Fig.12 which shows the width of satellites of different resonances along the line $a_y = a_x = a_\perp/\sqrt{2}$.

It is obvious that with the standard working point the 5th order resonances and their synchrotron satellites will lead to fast particle diffusion over the range of normalized betatron amplitudes from $a_\perp \approx 1.75$ to $a_\perp \approx 3.25$ affecting not only the pbar lifetime but the luminosity as well. To discuss possible cures some more insight is required.

Fig.13 shows contribution from all parasitic IPs to the $5\nu_x$ resonance driving term (RDT). It can be seen that only two points, just before two nominal IPs - B0 (IP#1) and D0 (IP#47) - provide significant contribution. These are the near-misses where the β-functions are $\beta_x \approx$ 151m, $\beta_y \approx$ 11m and the separation between the orbits is $|d_x| \approx 0.57$mm, $|d_y| \approx 1.13$mm. Contribution from the near-misses just after B0 and D0 where the ratio β_x/β_y is inverted, is by 3 orders of magnitude lower.

The resonance excitation can be reduced by increasing the total separation $d_0 = \sqrt{d_x^2 + d_y^2}$ and also by appropriate choice of the separation angle $\phi = \arctan(d_y / d_x)$ as illustrated by Fig.14.

An obvious solution would be to make separation completely vertical (and completely horizontal in the downstream near-misses) – then excitation of the odd-order resonances would be forbidden by symmetry. However, in this case the contribution to the horizontal tuneshift would reach its maximum (see Fig.14).

As seen in Figs.14, 15 the problem of near-misses can be significantly alleviated by a two-fold increase in the total separation and making the separation diagonal: $|d_x| \approx |d_y|$ as proposed for LHC Ref.[7].

4.2.3.2. Head-on interaction

An apparent cure would be to lower the tunes to get off the 5th order resonances. However, in this case pbars tunes will be well within the region of the 12th order

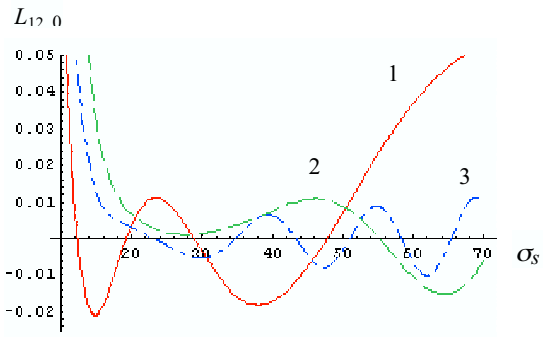

Figure 16. Longitudinal factor for 12th order resonances as function of bunch length σ_s (cm) at synchrotron amplitude $a_s = 1$ and chromaticity values: 1 - $\nu_\perp' = 0$; 2 - $\nu_\perp' = 6$; 3 - $\nu_\perp' = 12$.

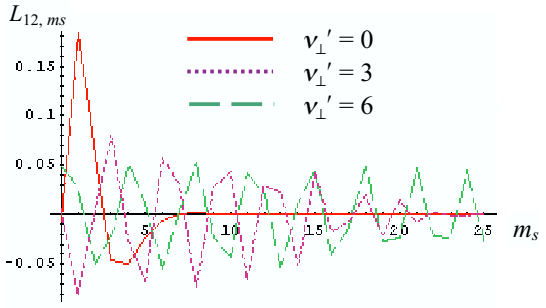

Figure 17. Longitudinal factor as function of the satellite number m_s at $a_s = 3$ and indicated values of chromaticity.

resonances which are driven mainly by the head-on interactions.

The head-on interactions provide by far the strongest nonlinear field that can drive even order resonances. However, due to a large ratio of the bunch length to β-function at IPs in Tevatron (design value $\sigma_s/\beta^* = 37/35$, actual value $\sigma_s/\beta^* = 60/35$), there is strong suppression of high order resonances in the result of phase averaging.

The phase averaging of even order resonances $2m = |m_x| + |m_y|$ in round beams with no offsets can be described by the longitudinal suppression factor (see Ref.[2]) which generalizes the Bessel satellite formula (13):

$$L_{2m,m_s}(a_s) = \mathrm{J}_{m_s}(2m\beta^*\eta\lambda a_s) + \int_0^\infty dt\, e^{-t-\lambda^2 t^2/8}\, \mathrm{J}_{m_s}[(2m\beta^*\eta - \frac{t}{2})\lambda a_s] \sum_{k=1}^{m} \frac{(-2)^k\, m!\, t^{k-1}}{(m-k)!(k-1)!k!}, \quad (19)$$

where $a_s = A_s/\sigma_s = \delta_{p0}/\sigma_p$ is relative synchrotron amplitude, $\lambda = \sigma_s/\beta^*$, $\eta = \nu_\perp'/\alpha_M R$ is chromaticity related parameter.

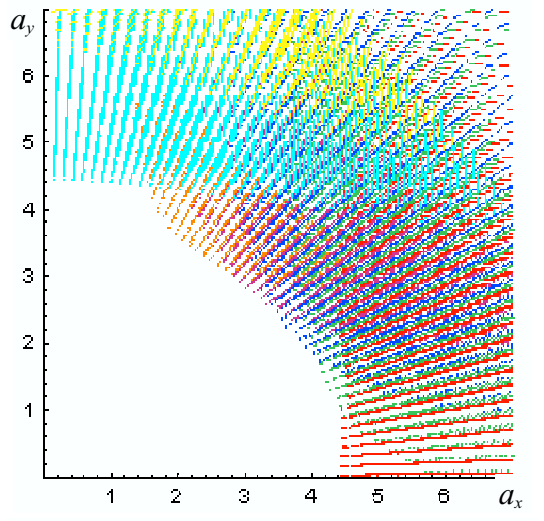

Figure 18. Swing of betatron amplitudes due to satellites of the 12th and 7th order resonances with lowered tunes 20.58, 20.75 at $\delta_{p0} = 3\cdot10^{-4}$ and $\nu_\perp' = 12$; reference emittance 15π mm·mrad.

Fig.16 shows this factor for 12th order principal resonances ($m_s = 0$) as function of bunch length σ_s at $a_s = 1$ and chromaticity values $\nu_\perp'$ increasing from 0 to 12. It can be seen that chromaticity noticeably reduces resonance excitation at $\sigma_s \sim 60$cm.

At the same time the chromaticity drastically increases the number of synchrotron satellites with the strength comparable to that of the principal resonance. Fig.17 shows the longitudinal factor of the satellites of the 12th order resonances at large synchrotron amplitude, $a_s = 3$, and three values of chromaticity.

The large number of strong satellites makes the effective width of the resonances very large. Fig.18 shows swing of the normalized transverse amplitudes in pbar

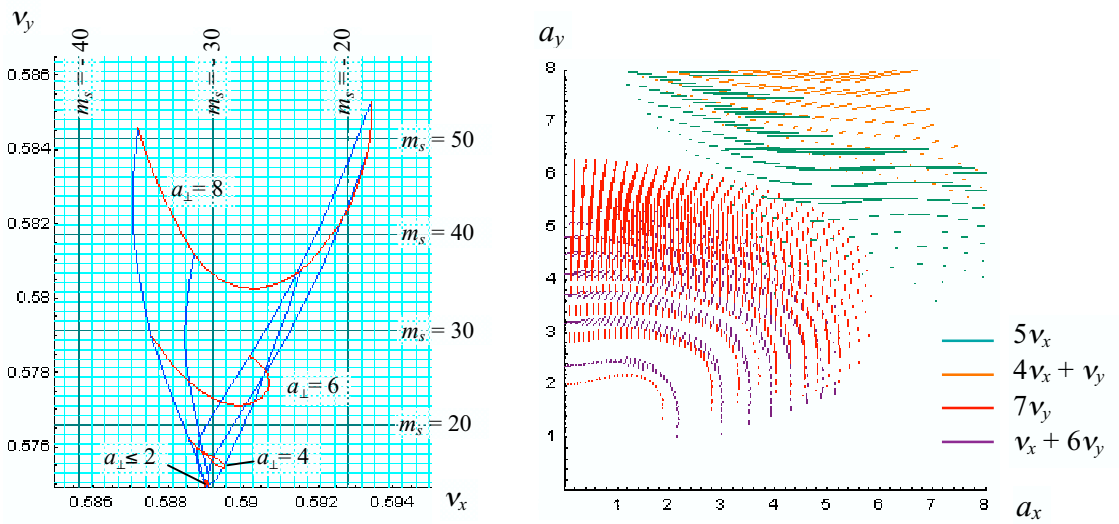

Figure 19. Footprint of pbar bunch #6 at injection on the grid of satellite lines of $5\nu_x$ and $7\nu_y$ resonances (left) and amplitude beatings due to satellites of the indicated resonances (right) at $\delta_{p0} = 7\cdot10^{-4}$ and $\nu_\perp' = 8$. Bare lattice tunes 20.585, 20.575, injection helix of 2001, reference emittance 15π mm·mrad.

bunch #6 on the 12th order resonances and their satellites at synchrotron amplitude $\delta_{p0} = 3\cdot10^{-4}$ ($a_s = 2$) and tunes $\nu_x = 20.58$, $\nu_y = 20.57$ lowered so as to avoid 5th order resonances. Also shown are the 7th order resonances excited mainly by the near-misses downstream the nominal IPs. Chromaticity in these calculations was set to 12.

There is a pronounced effect of $12\nu_x$ (red), $10\nu_x+2\nu_y$ (green), $8\nu_x+4\nu_y$ (blue), $6\nu_x+6\nu_y$ (violet), $4\nu_x+8\nu_y$ (orange), $\nu_x+6\nu_y$ (yellow) and $7\nu_y$ (cyan) resonances whose satellites overlap forming the region of fast dynamical diffusion starting from transverse amplitudes $a_\perp = (a_x^2 + a_y^2)^{1/2} \le 4.5$ (for emittance 15π mm·mrad).

Therefore the possibility of lowering the tunes at high proton intensities and high chromaticity is limited.

4.2.3.3. Beam-beam effect on protons

It is noteworthy that in the case when the nonlinear tuneshift is dominated by the beam-beam effect there is no dependence of the resonance width in the phase space on the intensity of the opposing beam (provided it is encountered at the same amplitudes) since both numerator and denominator in eq.(14) are proportional to it.

Therefore the protons are equally susceptible to the beam-beam resonances despite lower pbar intensity. In fact the effect on the protons can be even more detrimental due to smaller pbar emittance and therefore higher nonlinearity of the field they are creating. However at present small pbar intensity the satellites of the 12th order resonances for protons do not overlap so that no wide region of dynamical stochasticity is created.

4.2.3.4. Cures

There is a number of ways to alleviate the problem with beam-beam resonances in collision:

- Reducing the strength of the 5th order resonances (which are excited mainly by parasitic interactions nearest to the nominal IPs) by increasing separation with the help of additional separators and/or small crossing angle and optimizing the separation angle;
- Compression of the pbar tunespread with the help of electron lenses (nonlinear BBC);

♦ Lowering chromaticity (probably this will require octupoles to stabilize coherent modes).

4.2.4. Beam-beam resonances at injection, ramp and squeeze

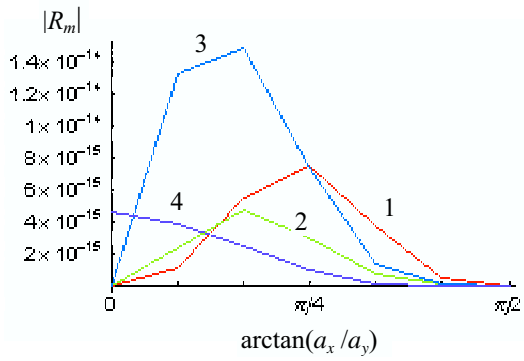

Figure 20. Driving terms of the 7th order resonances with the present injection helix as functions of the ratio of betatron amplitudes at $a_\perp = (a_x^2 + a_y^2)^{1/2} = 2$ with reference emittance 20π mm·mrad: 1 - $3\nu_x + 4\nu_y$, 2 - $2\nu_x + 5\nu_y$, 3 - $\nu_x + 6\nu_y$, 4 - $7\nu_y$.

There is a number of reasons which make beam-beam resonances no less dangerous at these stages than they are in collision despite absence of head-on interactions.

4.2.4.1. Beam-beam resonances at injection

The following circumstances contribute to beam-beam effect at injection:

a) separation between the beams is limited by available aperture (in some places by physical aperture, but generally by the dynamic one);

b) energy spread is much larger, $\sigma_p \approx (5 \div 6) \cdot 10^{-4}$, leading to strong synchro-betatron coupling despite lower chromaticity;

c) smaller vertical tuneshift with amplitude leaves pbars within the reach of the synchrotron satellites of the 7th order resonances.

The last two circumstances may increase the resonance excitation by machine nonlinearities as well (which already determine nonlinear tuneshift with the present injection helix). However, analysis of the nonlinear map with and without beam-beam interaction showed that the contribution of the machine nonlinearities to resonance excitation is small compared to the beam-beam interaction [8].

In the beginning of Run II the beam-beam resonances at injection proved to be a major limiting factor. Fig.19 from Ref.[9] shows the footprint of pbar bunch #6 and effect of the 5th and 7th order resonances at 150 GeV with 2001 injection helix and nominal proton beam parameters. One can see quite strong effect of the $\nu_x + 6\nu_y$ resonance as well, although the WP distance from it is larger than from the $7\nu_y$ resonance.

With the present helix design introduced in May 2002 the beam-beam resonances became much weaker, still they may affect pbar lifetime if the chromaticity is not low enough. Again, the $\nu_x + 6\nu_y$ resonance is the strongest, as comparison in Fig.20 shows. However, we use the strength of the $7\nu_y$ resonance as a figure of merit of helix design since this resonance is the nearest one to the working point.

There was a hope that after removal of C0 Lambertson magnets which presented the most severe restriction of the vertical aperture it would be possible to further reduce the beam-beam effects at injection. But the experimental studies showed that even employing all five separators which presently have polarity switches (two horizontal: B11H, B17H, and three vertical: B11V, C17V, C49V) it was not possible to achieve significant weakening of the beam-beam effects without increasing separation in other regions of limited physical and/or dynamic aperture.

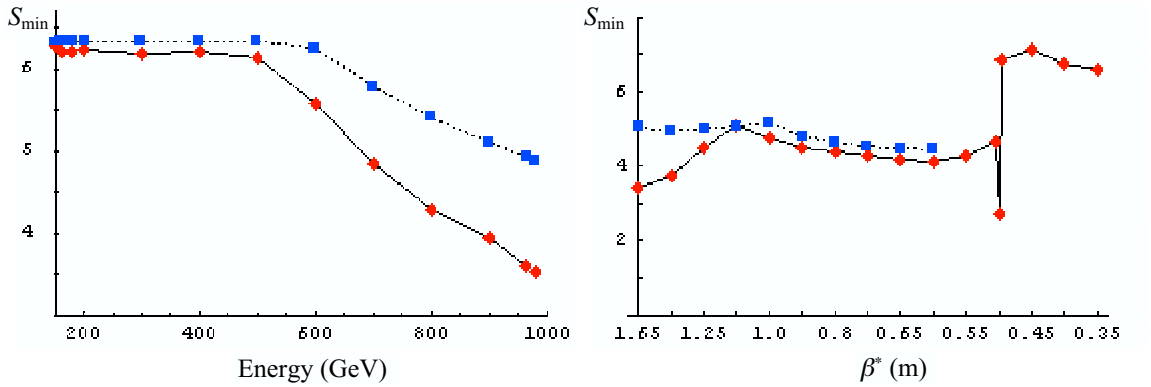

Figure 21. Minimum radial separation vs. energy on the ramp (left) and during the squeeze vs. β-function at nominal IPs (right) for the present helix (red diamonds) and one of the new versions (blue squares), reference emittance 15π mm·mrad

4.2.4.2. Beam-beam resonances at ramp & squeeze

In the end of the ramp/beginning of the squeeze the strength of the available at this step separators is not sufficient to provide the same relative separation (in $\sigma_{x,y}^{(\beta)} = \sqrt{\beta_{x,y}\varepsilon_{\text{r.m.s.}}}$) as at injection. However, the reduction can be made less dramatic by employing more separators.

Presently at this step the 2001 helix design is still effective which employs just two separators: B17H and C17V run at the maximum voltage of ±115.7 kV. Fig. 21 shows the improvement in the minimum value (over all 138 interaction points) of the radial separation S (see Eq.(1) for definition) during the ramp and squeeze which can be achieved by using all three vertical separators with polarity switches (additional ones with voltages in the beginning of the squeeze B11V= ±20.9kV, C49V= ±62.65kV).

Calculations of the beam-beam tuneshifts and resonance driving terms in the end of the ramp (EOR) with injection cogging and beginning of the squeeze (BOS) with collision cogging show significant improvement due to additional separators.

Table 4 presents the maximum values (over 12 pbar bunches in a train) of small-amplitude tuneshifts and $5\nu_x$ and $7\nu_y$ RDTs at betatron amplitudes of $3\sigma_x$ and $3\sigma_y$ correspondingly at injection, EOR and BOS with slightly reduced voltages ($U_{\max}$ =106.5 kV).

Table 4. Comparison of beam-beam effects at different steps with present and new helix designs

helix	step	$S_{\min}$	$\lvert\Delta\nu_x\rvert_{\max}$	$\lvert\Delta\nu_y\rvert_{\max}$	$\lvert R_{50}\rvert_{\max}\cdot 10^{12}$	$\lvert R_{07}\rvert_{\max}\cdot 10^{13}$
present	injection	6.33	.0028	.0019	1.47	0.28
	EOR	3.26	.0066	.0031	2.02	1.45
	BOS	3.09	.0078	.0031	2.33	2.54
new	injection	6.34	.0019	.0011	1.19	0.29
	EOR	4.46	.0033	.0016	1.07	0.31
	BOS	4.60	.0045	.0021	1.31	0.51

4.2.4.3. Beam-beam effects at squeeze sequence 16

During the squeeze B17H separator (which is the main horizontal separator at injection) must change its polarity. This helix rearrangement, which presently takes place at $\beta^* = 0.5$m (sequence 16), results in a significant drop in the separation.

In the beginning of Run II there were large pbar losses at this step resulting in decrease in luminosity with larger proton intensity. In March 2002 a solution was found providing a 50% larger separation at the minimum point. This solution, together with increased slew rate of feeddown sextupoles, allows to pass this step without noticeable pbar losses.

A further moderate improvement can be achieved just by temporarily increasing the separator voltages at this step.

The search is underway for a principally new solution employing larger number of separators as discussed in the corresponding section.

4.2.5. Effect of beam-beam interaction on beam emittance evolution and lifetime

Although resonance widths characterize the strength of the beam-beam effects they are not directly related to the particle loss and emittance growth in the collider. Unlike the electron-positron colliders there is no suppression of dynamic diffusion by synchrotron radiation (SR) damping in the hadron colliders. That results in a requirement that the resonances should not overlap in a fashion allowing a particle to be transported from small amplitudes to the machine aperture by dynamic diffusion. In practical terms it usually limits the total linear tune shift by ~0.02 – 0.03. Because of absence of SR damping there is long-term memory in the beam and therefore tracking for very large number of turns is a major way to understand effects of no-linearities on the evolution of beam distribution. But direct tracking is presently limited to a few million turns, which represent only about 1 minute of beam life in Tevatron. Nevertheless hierarchy of time scales in the problem allows one to decompose effect of different phenomena and compute the beam lifetime and particle loss for the entire store duration.

There are three important time scales related to the particle loss and emittance growth in the collider. The first one is period of oscillations inside resonance islands. It depends on the resonance order and strength, and usually ranges between few hundred and few thousand turns. The second one is the time of the resonance driven diffusion between overlapped resonance islands. It is slower than the motion inside resonance but still is much faster than the time related to IBS and other non-dynamic diffusion mechanisms discussed in Section 3. Although this third time scale is very slow (~10^8 turns) comparing to the first two, it actually determines the beam parameters evolution during the store. In this case the beam-beam interaction and lattice non-linearities facilitate the "external" diffusion but are not the primary mechanisms of particle loss and emittance growth. Note that this picture is completely different from electron-positron colliders where the particle to be lost must travel from small to large amplitudes during one SR damping time of few thousand turns.

To describe particle motion in the presence of nonlinear fields and diffusion we start from Vlasov equation written for normalized coordinates and velocities,

$$\frac{\partial f}{\partial t} + \mathbf{v}_i \frac{\partial f}{\partial \mathbf{x}_i} + \left(-\omega_i^{\,2}\mathbf{x}_i + \widetilde{F}_i(\mathbf{x}_i, t) \right) \frac{\partial f}{\partial \mathbf{v}_i} = \frac{\partial}{\partial \mathbf{v}_i} \left(D_{ij}(\mathbf{x}_i, \mathbf{v}_i, t) \frac{\partial f}{\partial \mathbf{v}_j} - F_i(\mathbf{x}_i, \mathbf{v}_i, t) f \right) \quad .(20)$$

Transformation to the action-phase variables and averaging over phases yields

$$\frac{\partial f}{\partial t} - \frac{\partial}{\partial \mathbf{I}_i}\left(\widetilde{D}_{ij}(\mathbf{I})\frac{\partial f}{\partial \mathbf{I}_j} - \widetilde{F}_i(\mathbf{I}) f \right) = \frac{\partial}{\partial \mathbf{I}_i}\left(D_{ij}(\mathbf{I})\frac{\partial f}{\partial \mathbf{I}_j} - F_i(\mathbf{I}) f \right) \quad . \qquad (21)$$

Here the diffusion and friction are related to the non-linear dynamics in the left-hand side and to the actual diffusion on the right-hand side. The only friction force is due to IBS. It is negligible comparing to diffusion for Tevatron parameters and therefore we finally can write that

$$\frac{\partial f}{\partial t} = \frac{\partial}{\partial \mathbf{I}_i}\left(\left(D_{ij}(\mathbf{I}) + \widetilde{D}_{ij}(\mathbf{I}) \right) \frac{\partial f}{\partial \mathbf{I}_j} \right) \quad . \qquad (22)$$

The solution of this equation is strongly simplified by the fact that the dynamic diffusion $\widetilde{D}_{ij}(\mathbf{I})$ is much larger than the "external" diffusion $D_{ij}(\mathbf{I})$. In this case we can put $\widetilde{D}_{ij}(\mathbf{I})$ to infinity inside resonance islands and to zero outside.

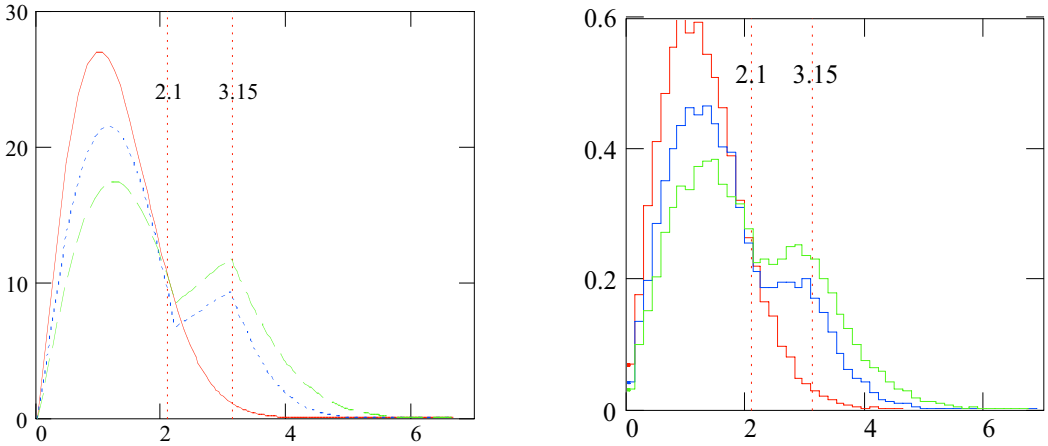

Figure 22. Distribution function evolution under combined effect of noise and beam-beam interaction in vicinity of 6-th order resonance, ν=0.325, ξ=0.02 with one IP, $\Delta p/p$=0, $\sigma_s << \beta^*$; red line – initial distribution, blue line – after 5000 turns, green line – after 10000 turns. Left figure is obtained by tracking of 20,000 particles for 10,000 turns. Right figure is obtained by solving Eq. (22) with resonance width found by tracking (see Figure 23).

To verify accuracy of the described above model we compared its prediction with results of particle tracking in the presence of beam-beam interaction and external noise. Figure 1 presents results in the form of distribution function $F(r)$ over phase space radius r so that it is bound to the distribution function by the following equation $F(r) = r\,f(r)$.

In the case of tracking the phase space radius is determined by the following equation

$$r = \sqrt{x^2 + \left(1 + 2\pi\kappa\xi / \tan(2\pi\nu)\right)^2 p^2}\ , \ \kappa \approx 1, \qquad (23)$$

where the term proportional to the linear tune-shift ξ is introduced to correct a distortion of

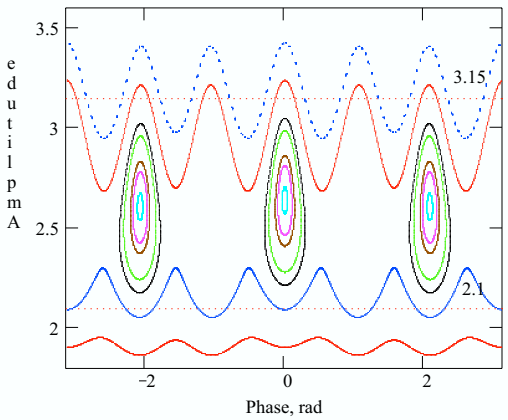

Figure 23. Phase trajectories in vicinity of 6-th order resonance with beam parameters of Figure 22.

phase space trajectories introduced by the linear part of beam-beam force. The tracking was performed in vicinity of 6-th order resonance for bunches of zero length and one IP with the linear tune shift ξ=0.02. It increased the resonance width and the frequency of particle motion inside resonance island and, consequently, allowed to demonstrate the effect of the resonance clearly with only 20,000 particles and 10,000 turns. For chosen parameters the period of oscillations inside resonance island N_{isl} ranges from ~150 turns at small amplitude to ~250 turns at large amplitude. The noise was simulated by random jumps in the phase space at every turn. The initial distribution function was gaussian with σ = 1. The rms value of jumps of 0.01 was chosen so that after 10,000 turns the beam emittance would be doubled. In average after one revolution around resonance island such noise randomly displaces the particle by $\Delta\sqrt{N_{isl}} \approx 0.15$ which is about 6 times smaller than the island width. In this case particle transport from one to another side of the island mainly occurs due to dynamic motion while diffusion is responsible for particle transport outside the resonance. That is a necessary condition for correct description of the particle diffusion through the resonance island.

The right hand part in the Figure 1 presents results of numerical solution of Eq. (22) with resonance boundaries taken from particle tracking in vicinity of resonance (see Figure 23). One can see that there is quite close coincidence in spite the fact that we neglected actual shape of resonance islands in solution of Eq. (22). It resulted in the sharp angles on the right-hand picture of Figure 22. Figure 24 presents the dependence of rms beam emittance on time obtained by solving Eq. (22). There are three different time scales determining the beam size evolution. The first one is related the period of oscillations in the resonance islands, which levels the distribution function after few thousand turns. It causes instant jump of emittance in Figure 24. Then the distribution function around the resonance islands comes to local equilibrium with time constant determined by the resonance width Δ, $\tau \approx \Delta^2 / 4D \approx 0.25$. Finally, the emittance grows linearly with time, but the emittance growth rate is amplified by resonance by factor ~1.5.

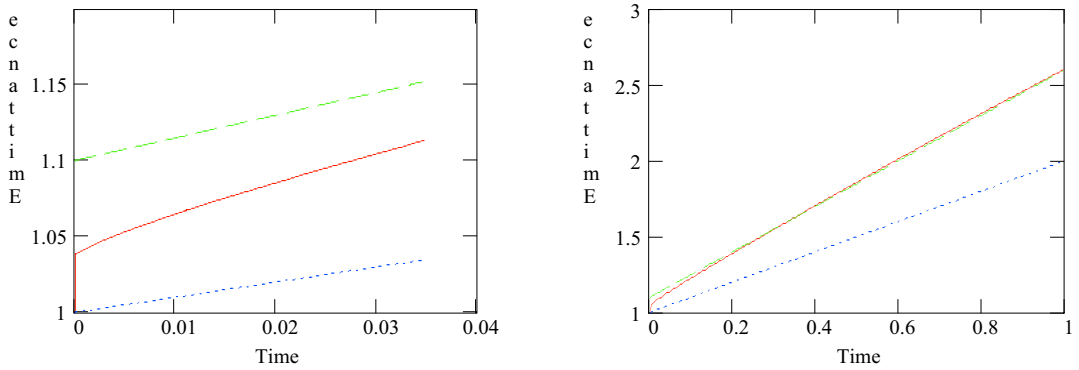

Figure 24. Dependence of the rms emittance on time obtained by numerical solution of Eq. (22) with parameters of Figure 1; solid line – results of simulations, dotted line – presents results in the absence of beam-beam effects, dashed line – linear dependence presenting emittance growth for large time, ε=1.1+1.5t.

In the general case Eq. (22) need to be solved in the three-dimensional space of actions with beam-beam diffusion depending on all three actions. It requires computing boundaries for all resonances; the problem that is not much simpler than direct tracking for millions turns. However described above picture puts insight how the beam-beam

effects work during store. It also determines how reliable simulation of beam-life time and particle loss can be performed. To achieve accuracy of about 10% in computations of beam lifetime the resonances with width more than $\sim 0.1\sigma$ need to be correctly represented. The period of oscillations in resonance islands for resonances of 12-th order is quite slow and usually is about 2000 – 4000 turns. A requirement that the noise should not transport particle by more than 15% of resonance width during one revolution around the island sets the noise step size per turn to be $0.1 \cdot 0.15 / \sqrt{3000} \approx 3 \cdot 10^{-4}$. That yields that after 10^6 turns the beam size will grow by 30% and the emittance by factor ~1.7. Depending on beam current that represent 10 to 100 hours of real beam life. We plan to start such simulations soon and the first results are expected by the end of 2003.

4.3. Coherent beam-beam effects

In this section we will discuss what impact the beam-beam interaction may have on stability of coherent motion, in particular:

- Landau damping by the tunespread in proton and pbar beams introduced by the beam-beam interaction;
- Possibility of appearance of discrete spectral lines of coherent beam-beam oscillations (undamped by the beam-beam tunespread) with increasing number of pbars;
- Resonances of coherent beam-beam oscillations.

Also, we will discuss two major mechanisms of suppression of coherent beam-beam oscillations: tunesplit between the interacting beams and Landau damping by overlapping synchrotron sidebands on incoherent betatron tunes.

4.3.1. Landau damping by the beam-beam tunespread

The high intensity proton beam in the Tevatron is prone to coherent instabilities at all times starting from injection until the beams are put into collision (and sometimes even after that).

So far the main remedy from the transverse instabilities was high positive chromaticity (+8 at injection, +(16÷20) during ramp, squeeze and in collision) which provides damping of the dipole modes. Recently digital transverse dampers were made operational during pbar injection allowing to reduce chromaticity by ~ 4 units. However, positive chromaticity may provoke transverse head-tail instability incurable with dampers.

The main mechanism of stabilization of the transverse modes is Landau damping due to spread in betatron and (for the head-tail modes) synchrotron tunes. At top energy the beam-beam interaction is the major source of the tunespread in both beams.

The theory of Landau damping in the case of limited tune variation requires some comments.

4.3.1.1 The Liouville-Vlasov equation

We make the conventional choice of the generalized azimuth $\theta = s/R$ as the independent variable and the action-angle variables $\underline{I} = (I_x, I_y, I_s)$, $\underline{\psi} = (\psi_x, \psi_y, \psi_s)$ as canonical variables; by the action variables we understand the renormalized invariants of motion with account of the beam-beam interaction and chromaticity (and divided by the r.m.s. emittance, so that their mean values equal 1).

The invariants of motion can be used in construction of the equilibrium distribution function which we presume to be Gaussian:

$$F_0(\underline{I}) = e^{-(I_x + I_y + I_s)} \tag{1}$$

To simplify the formulas let us limit ourselves to one-dimensional problem. Small perturbations of the distribution function $F_1(I_x, \psi_x; \theta)$ are governed by the linearized Liouville-Vlasov equation which we will cast into the form

$$\begin{aligned} i\frac{\partial F_1}{\partial \theta} &= \hat{A} F_1, \\ \hat{A} F_1 &= -i\nu_x(\underline{I})\frac{\partial F_1}{\partial \psi_x} - i\frac{\partial F_0}{\partial I_x}\dot{I}_x(F_1), \end{aligned} \tag{2}$$

where $\dot{I}_x(F_1)$ is the response to the perturbation from external impedances and/or the counter-rotating beam.

Also, we will consider only dipole oscillations, $F_1 \sim \exp(i\psi_x)$. Let us note that in the case of a large tunespread the beam does not oscillate as a whole (when $F_1(I_x) \sim \sqrt{I_x}\,\partial F_0 / \partial I_x$), the dependence on I_x may be arbitrary.

4.3.1.2 The Case-Van Kampen modes

The general approach to stability analysis is to find the eigensystem of the operator $\hat{A}$:

$$\hat{A}\Psi_\lambda = \lambda\,\Psi_\lambda \tag{3}$$

which may present insurmountable difficulties. We will proceed in steps starting from the simplest case when the second term in operator A can be neglected (no impedances, weak response from the counter-rotating beam due to e.g. large tunesplit).

Then in the considered case of dipole oscillations this operator is just multiplication by the tune: $A = \nu_x(I_x)$, for λ belonging to the range of ν_x its eigenfunctions are the Dirac δ-functions

$$\begin{aligned} \Psi_\lambda(I_x) &= \sqrt{\frac{F_0(I_\lambda)}{|\nu_x'(I_\lambda)|}}\,\delta(I_x - I_\lambda), \quad \lambda \in (\nu_{x0}, \nu_{x0} + \xi_x), \\ \nu_x(I_\lambda) &= \lambda\,, \end{aligned} \tag{4}$$

where the normalization constant was chosen so that the eigenfunctions were orthonormal with weight $F_0^{-1}(I_x)$ (this will be convenient in the general case of beam-beam interaction).

$$\int_0^\infty \Psi_\lambda(I_x)\Psi_\mu(I_x)\frac{dI_x}{F_0(I_x)} = \ddot{a}(\lambda-\mu) \qquad (5)$$

In our simple example operator $\hat{A}$ has only continuous spectrum, the eigenmodes belonging to such spectrum are sometimes called the Case-Van Kampen modes.

The general solution to the Liouville equation can be presented as expansion

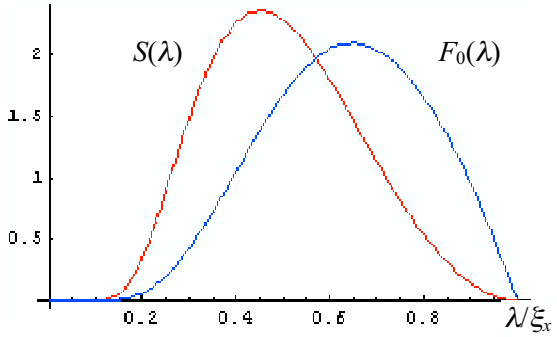

Figure 1. Spectral density of dipole oscillations (red) and distribution in incoherent tunes (blue) in head-on colliding round beams.

$$F_1(I_x;\theta) = \frac{1}{\sqrt{2}}\int e^{-i\lambda\theta}c_\lambda\Psi_\lambda(I_x)d\lambda\,, \qquad (6)$$

in the particular case of oscillations excited by a dipole kick of unit amplitude (in beam $\sigma_{x'}$)

$$c_\lambda = \int_0^\infty \Psi_\lambda(I_x)\sqrt{I_x}\,dI_x\,. \qquad (7)$$

These expansion coefficients have an important property (the Parseval identity)

$$\int c_\lambda^2 d\lambda = 1\,. \qquad (8)$$

The center-of-mass oscillations after the unit kick

$$\frac{x_{\text{c.m.}} + i(\beta_x p_{x\,\text{c.m.}} + \alpha_x x_{\text{c.m.}})}{\sigma_x} = \int_0^\infty F_1(I_x;\theta)\sqrt{2I_x}\,dI_x = \int e^{-i\lambda\theta}c_\lambda^2 d\lambda \qquad (9)$$

have the spectral density $S(\lambda)=c_\lambda^2$ which in our simple example can be found analytically from eqs.(4,7,9):

$$S(\lambda) = \frac{I_\lambda F_0(I_\lambda)}{|\nu_x'(I_\lambda)|} \qquad (10)$$

It has the same form as the Schottky power density in low frequency bands (see e.g. Ref.[10]), the coincidence is owing to the Gaussian distribution function.

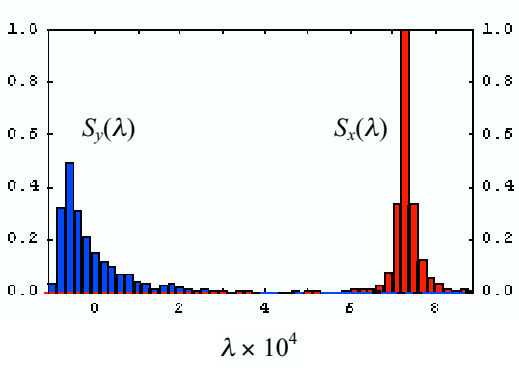

Figure 2. Spectral density of horizontal (red) and vertical (blue) oscillations in p-bunch #3 as function of $\lambda = \nu_{x,y} - \nu_{x,y0}$ in the beginning of flat-top (squeeze step 1) with $N_{\bar{p}} = 3 \cdot 10^{10}$.

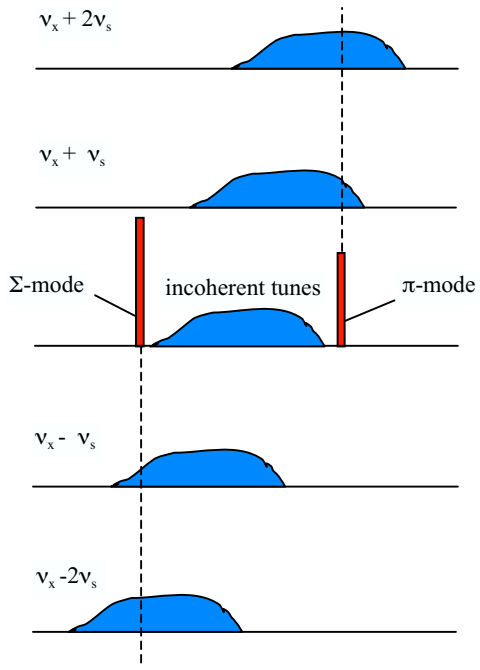

Figure 3. Schematic of oscillations spectrum it two colliding bunches of comparable intensity

4.3.1.3 Landau damping

Now we can take into consideration external impedances which deliver dipole kicks proportional to the center-of-mass displacement. Let these impedances in the absence of the tunespread produce the coherent tuneshift $\Delta\nu_{coh}$, generally complex. If $\mathrm{Im}\Delta\nu_{coh} > 0$ the beam is unstable.

In the presence of the tunespread the coherent tune λ is determined by the dispersion relation, which in the case of weakly coupled (e.g. due to tunesplit) oscillations has the form

$$1 - \Delta\nu_{coh} \int \frac{c_\mu^2 d\mu}{\lambda - \mu} = 0 , \qquad (11)$$

coincident with that of eq.(5.52) of Ref.[11]. The latter contains in the integrand the distribution function in incoherent tunes $F_0(\lambda)$ instead of the spectral density $S(\lambda)=c_\lambda^2$. The difference arises from a different nature of the tunespread assumed in Ref.[11].

In the one-dimensional Gaussian model $S(\lambda)$ is given by eq.(10) and differs from the distribution function in incoherent tunes $F_0(\lambda)$

$$F_0(\lambda) = \frac{F_0(I_\lambda)}{|\nu_x'(I_\lambda)|} \qquad (12)$$

by additional multiplier I_λ.. The two functions for the case of head-on collisions of round beams are shown in Fig.1.

The formal identity of the dispersion relations permits to apply the results obtained in Ref.[11] to our case. Then from the simplified stability criterion (5.62) of Ref.[11] for the shown in Fig.1 spectral width we get

$$|\Delta\nu_{coh}| < \frac{\Delta\lambda_{1/2}}{\sqrt{3}} \approx \frac{0.21\xi_x}{\sqrt{3}} \approx 0.12\xi_x . \qquad (13)$$

The coherent tuneshift at top energy can be estimated as $|\Delta\nu_{coh}| \sim 10^{-4}$. The tunespread in the proton beam in collision even with such small amount of pbars/bunch as

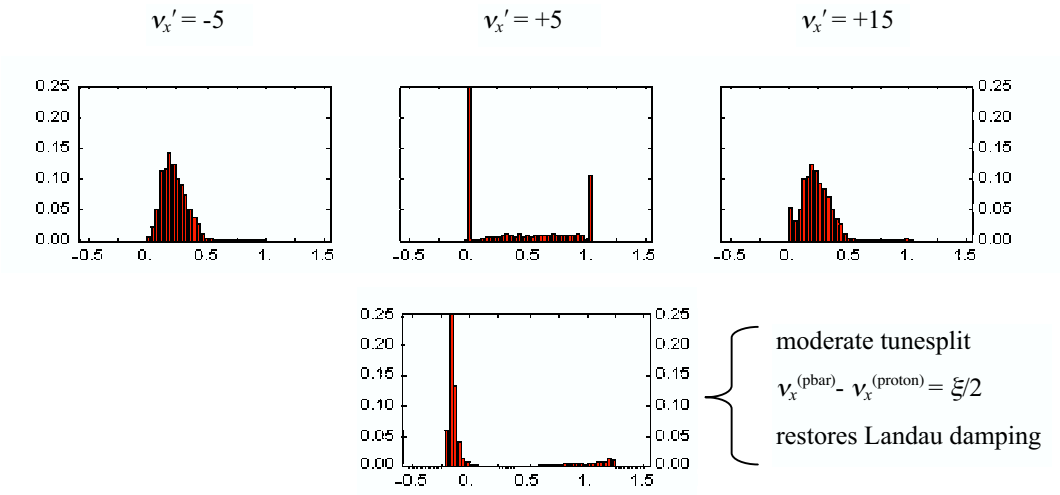

Figure 4. Effect of chromaticity and tunesplit on oscillations spectrum in two colliding bunches of finite length $\sigma_s/\beta^* = 50/35$ with synchrotron tune $\nu_s/\xi_x^{(pbar)} = 0.035$ and intensity ratio $N_{\bar{p}}/N_p = 1/2$ (abscissa values in $\xi_x^{(pbar)}$).

$N_{\bar{p}} = 3\cdot 10^{10}$ (which provides $\xi_x \approx 0.0025$) should be (marginally) sufficient for suppression of the dipole transverse instability.

However, before the beams are put into collision the proton tunespread is too small, especially in the horizontal plane as Fig.2 shows for proton bunch #3 at the squeeze step 1. Probably this is the reason why the horizontal instability is regularly observed in the beginning of flat-top.

4.3.2. Discrete modes of coherent beam-beam oscillations

Increasing pbar intensity will make the proton incoherent tunespread wider but this does not automatically guarantee Landau damping. On the contrary, when the intensity ratio exceeds 0.6 sharp spectral lines of coherent beam-beam oscillations may appear (see Ref.[12]).

The response of pbar beam to the proton beam perturbation adds to operator $\hat{A}$ of eq.(2) an integral term with the two-dimensional electrostatic Green function as the kernel (in fact we should consider the full problem described by a system of Liouville-Vlasov equation for all interacting bunches, see Refs.[12-14] for details).

This integral operator has a discrete set of eigenvalues, so that the total operator may have a mixed spectrum: the Case-Van Kampen continuum which reproduces the incoherent tunespread and some number of undamped discrete lines.

4.3.2.1. Coherent modes in two head-on colliding bunches

When intensities of colliding bunches are (approximately) equal there are two families of modes of mutual oscillations: Σ-modes when the bunches oscillate in phase and π-modes when the phases of their oscillations are opposite. As found in Ref.[13], the spectrum of each family contains the continuum of incoherent tunes and discrete lines. The total spectrum is shown schematically in Fig.3.

In short bunches the discrete Σ-mode has unshifted bare lattice tune, $\lambda = 0$, since the

bunches do not see each other's displacement; this is a truly rigid-body motion.

The discrete π-mode has tuneshift exceeding maximum incoherent tuneshift, in round beams [13]

$$\lambda_{\pi} = 1.214\xi_x \tag{14}$$

The effect of external impedances is still described by dispersion relation (11) where the integral should be understood now as the Stieltjes integral: a sum over the discrete eigenvalues and the integral over the continuum.

Since the discrete lines are well separated from the continuum they generally are not Landau damped, the beam-beam interaction only slightly reduces instability growth rate of the π-mode (see Ref.[12] for more discussion). However, Landau damping naturally occurs in finite length bunches due to synchrotron sidebands overlap (Ref.[14]) and can be further enhanced by adjustment of chromaticity and splitting the bare lattice tunes in two beams (Ref.[15]).

For synchrotron sidebands overlap to occur (as illustrated by Fig.3) the synchrotron tune should be smaller than but not negligibly small compared to the beam-beam parameter which is true for Tevatron. Just as in the case of incoherent synchro-betatron coupling described by eq.(4.19) of the previous Section, there is an interference between effects of chromaticity and finite bunch length at IP.

At small bunch length ($\sigma_s/\beta^* \ll 1$) the net damping effect is determined by the coupling parameter

$$\kappa = (\nu'_x/\alpha_M R - 1/\beta^*)^2 \sigma_s^2 \tag{15}$$

which tends to zero at the chromaticity value

$$\nu'_{x,y} = \alpha_M R/\beta^* \approx 8. \tag{16}$$

The case of bunch length comparable to β^* was treated in Ref.[16].

Landau damping can be visualized as the width of discrete lines in the spectra. The upper row in Fig.4 presents the result of computation of the beam-beam spectrum (in the simplified case of flat beams at IP) at three values of chromaticity. When the chromaticity is close to the value given by eq.(16) the discrete modes are clearly seen, but are completely submerged into the continuum when the chromaticity is sufficiently far from this value.

Even with unfavorable values of chromaticity Landau damping can be restored by splitting the bare lattice tunes in two beams by an amount $\geq \xi_x^{(\mathrm{pbar})}$, as the lower plot in Fig.(4) demonstrates. These two methods of enhancement of Landau damping should be enough to ensure the coherent stability of head-on colliding bunches. However, the multiple long-range interactions may change the picture.

4.3.2.2 Coherent modes in multiple bunches

There are three trains of 12 bunches in each beam, so that each bunch experiences 72 interactions with the counter-rotating beam. Since the gap between two trains (119 RF buckets) is not a multiple of bunch spacing (21 RF buckets) the points where the bunches of different trains interact are all different, therefore there are total of 138 interactions points.

To get an idea of how the spectrum of coherent oscillations in such complicated

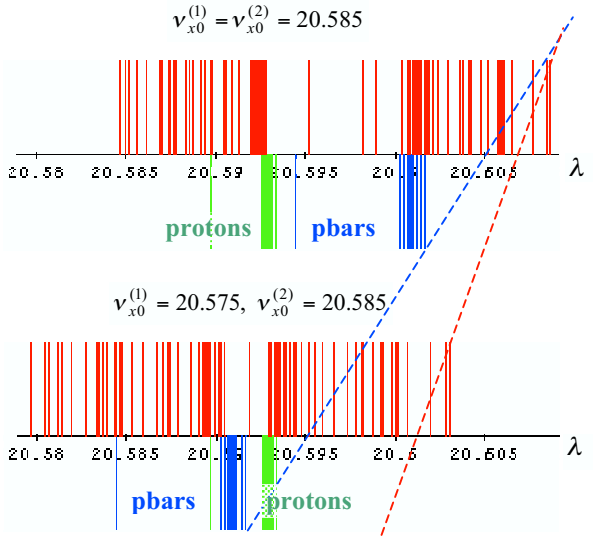

Figure 5. Spectral lines of coherent modes in 36x36 bunches (upper red lines) and average values of incoherent tunes in proton bunches (lower green lines) and pbar bunches (lower blue lines) at equal bare lattice tunes (top) and with tunesplit of 0.01 (bottom).

system may look let us assume the bunches to be rigid and linearize the beam-beam kicks w.r.t. the center-of-mass displacement. For long-range interactions we may assume all particles in the bunch to get the same kick as the central particle, whereas for head-on interactions we must take average values which are twice smaller than the kick received by the central particle.

It is convenient to use complex normal form variables, $a_k^{(b)}$, to describe the center-of-mass motion of the bunches:

$$x_k^{(b)} = \sqrt{\beta_x(\theta)/2}\, e^{i\phi_x(\theta)} a_k^{(b)}(\tau) + \text{c.c.} \tag{17}$$

where k is the bunch number, b is the beam number (let pbars be the first beam and protons the second), $\phi_x(\theta) = \mu_x(\theta) - \nu_{x0}\theta$ is periodic phase advance. Azimuthal position of the bunch can be expressed via the common "time" τ as $\theta = (-1)^b(\tau - \vartheta_k)$ where ϑ_k is the lag w.r.t. the first bunch of the corresponding beam.

Tevatron tunes $\nu_{x,y}$ are close to half-integer values; to have a possibility to study coherent half-integer resonance let us include into analysis coupling via the beam-beam potential with the mirror symmetric modes, $n - \nu_{x,y}$, where $n = \text{Round}[2\nu_{x,y}]$. In the linear approximation the equations of motion become (we neglect transverse coupling and write equations for one plane only)

$$\begin{aligned} i\frac{d}{d\tau}a_k^{(1)} &= \nu_{xk}^{(1)} a_k^{(1)} - \sum_{IP} \chi_{IP} N_{\bar{k}}^{(2)} [e^{-2i\phi_{IP}} a_{\bar{k}}^{(2)*} + e^{-in(\tau-\vartheta_k+\theta_{IP})}(a_{\bar{k}}^{(2)} - e^{-2i\phi_{IP}} a_k^{(1)*})], \\ i\frac{d}{d\tau}a_j^{(2)} &= -\nu_{xj}^{(2)} a_j^{(2)} + \sum_{IP} \chi_{IP} N_{\bar{j}}^{(1)} [e^{-2i\phi_{IP}} a_{\bar{j}}^{(1)*} + e^{in(\tau-\vartheta_j-\theta_{IP})}(a_{\bar{j}}^{(1)} - e^{-2i\phi_{IP}} a_j^{(2)*})], \end{aligned} \tag{18}$$

where the asterisk means complex conjugation, $\bar{k}$ is the number of the bunch in the

counter-rotating beam which collides with bunch k at a given IP, χ_{IP} is one particle contribution to the incoherent tuneshift at the given IP, $\nu_{xk}^{(b)}$ are incoherent tunes with beam-beam contribution included.

To get rid of the explicit dependence on τ we can introduce new variables

$$u_k^{(1)} = a_k^{(1)*},\ u_k^{(2)} = a_k^{(2)},\ v_k^{(1)} = e^{in\tau} a_k^{(1)},\ v_k^{(2)} = e^{in\tau} a_k^{(2)*}, \tag{19}$$

and solve the eigenvalue problem for the system of 144 autonomous differential equations.

Results obtained with bunch intensities $N_{\bar{p}} = 1.35 \cdot 10^{11}$, $N_p = 2.7 \cdot 10^{11}$ are presented in Fig.5 in the form of line spectra (upper red lines). For comparison average values of incoherent tunes in proton and pbar bunches are shown with lower green and blue lines. We should remind that the maximum incoherent tuneshift due to head-on interactions is approximately twice larger than the average value, so that we should add 0.01 to pbar incoherent tunes and 0.005 to proton tunes.

Taking this into account we can see that if the bare lattice tunes are equal the coherent lines are within the incoherent tunespread and should be Landau damped. However, if the bare lattice tune for pbars is by 0.01 lower (which is presently the case in Tevatron), then the highest coherent tune is by ≈ 0.003 out of the incoherent tunespread. This distance can be covered only by synchrotron sidebands of order ≥ 5, Landau damping provided by such high order sidebands may be not sufficient for stability.

Let us note in conclusion of this section that the analysis shows that the coherent half-integer resonance mentioned earlier does not present real danger unless the tunes are too close to 20.5 (e.g. vertical oscillations at step1 may become unstable at cited above intensity if $\nu_{y0} < 20.538$).

4.4. Experimental and numerical studies of the beam-beam effects

4.4.1. Injection

Similar to high-energy stores the beam evolution at injection is governed by interplay of beam-beam effects and diffusion. For the present typical beam parameters (emittances of 20 mm mrad, the rms bunch length of 1 m, the intensities of $3\cdot10^{11}$ and $3\cdot10^{10}$ for proton and antiproton beams, correspondingly) and the residual gas composition the same as in Section 3 one can estimate the emittance growth rates to be: $d\varepsilon_x/dt \approx d\varepsilon_y/dt \approx 1.3$ mm mrad/hour for multiple gas scattering, $d\varepsilon_x/dt + \varepsilon_y/dt \approx 3$ mm mrad/hour for IBS in the proton beam, and $d\varepsilon_x/dt + d\varepsilon_y/dt \approx 0.3$ mm mrad/hour for IBS in the antiproton beam. That causes 5 – 10% emittance growth during shot setup ~1 hour time. There is also strong IBS diffusion for longitudinal degree of freedom in the proton beam. If the bunch lengthening would not be limited by finite size of the RF bucket the longitudinal emittance lifetime would be ~25 hours. Although the emittance growth rates are sufficiently small they cause significant beam lifetime deterioration due to dynamic aperture limitations and finite size of RF bucket.

Similar to the high energy stores there are hierarchy of time scales: (1) fast particle loss due to non-linear resonances (≤ 1-10 s), (2) relaxation of sharp perturbations in the distribution function due to beam heating (~ 10 s – 10 min), and (3) slow diffusive decay of beam intensity (~ 10 min – many hours). Usually aperture is more limited in one plain than in another, and we can consider one-dimensional model to describe the particle loss due to diffusion. In this case the diffusion equation,

$$\frac{\partial f}{\partial t} = \frac{\partial}{\partial I}\left(ID\frac{\partial f}{\partial I}\right) , \qquad (1)$$

needs to be solved with boundary condition $f(t,I_0) = 0$, where I_0 is the machine acceptance. A solution of the equation can be written in the following general form

$$f(t,I) = \sum_{n=0}^{\infty} A_n \exp\left(-\frac{Dt}{4I_0}\mu_n^{\,2}\right) \mathrm{J}_0\left(\mu_n\sqrt{\frac{I}{I_0}}\right) . \qquad (2)$$

Here A_n are the coefficients determined by the initial distribution, and μ_n are the n-th root of the zero order Bessel function $\mathrm{J}_0(x)$. The zero term has the slowest decay and will dominate solution at large times, where the system comes into an equilibrium. Then the intensity decays with time as $\tau_\infty = 4I_0/\left(D\mu_0^{\,2}\right)$, $\mu_0 \approx 2.405$, the shape of the distribution is not changing with time $f(t,I) \propto \mathrm{J}_0\left(\mu_0\sqrt{I/I_0}\right)$, and rms emittance is

$$\varepsilon_\infty \approx 0.09 I_0 \quad . \qquad (3)$$

Taking into account that $d\varepsilon/dt = D/2$ we obtain for intensity decay time

$$\tau_\infty = 2I_0/\left(\mu_0^{\,2} d\varepsilon/dt\right) \quad . \qquad (4)$$

For emittance growth rate[4] of 1.3 mm mrad/hour and the acceptance of 53 mm mrad (4σ of 20 mm mrad emittance) we obtain the beam intensity lifetime of 13 hour. If the initial

[4] We remind that all numerical values of emittances used in the paper are the 95% emittances determined as 6 times of rms emittance. The rms emittances are used in all formulas through the paper.

beam emittance is smaller than ε_∞ then the initial intensity lifetime will be higher than τ_∞ and otherwise if smaller.

The beam lifetime at the central orbit is usually a few hundred hours, but it strongly deteriorates after particles moved to their helical orbits. The antiproton beam lifetime is additionally affected by the beam-beam interaction. Figure 1 presents the dependence of antiproton beam lifetime on the vertical emittance for the case when antiprotons are on their helical orbit and there are no protons in the ring. As one can see the lifetime varies between 10-25 hours compared to lifetimes of 1-10 hours in stores, and it is strongly correlated with the vertical emittance. The losses during acceleration were also small, about 2%, compared to typical losses around 10% in stores. Presented in Figure 1 dependence of lifetime on the emittance and its numerical value are consistent with the above estimate for particle loss due to the diffusive beam heating in the aperture-limited ring. More detailed measurements are required to find precise values of the machine acceptance and diffusion.

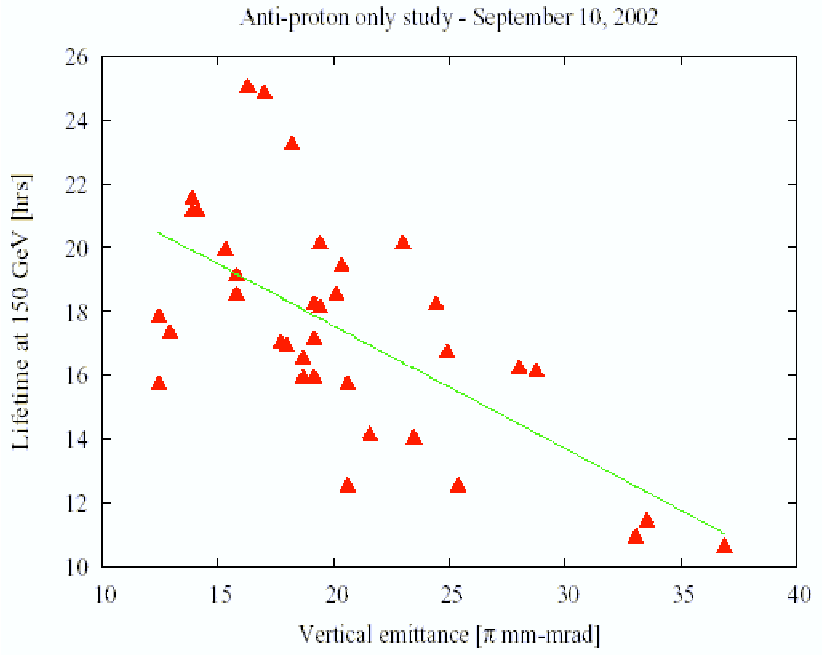

Figure 1. Lifetime of antiproton bunches in an antiproton only dedicated experiment as a function of the vertical emittance (courtesy F. Schmidt); measurements were performed in September 2002.

In order to understand the influence of the beam-beam interactions, the dynamic aperture of a few antiproton bunches at 150 GeV has been calculated with extensive simulations. The nonlinearities in the model include the measured multipoles in the magnets, the chromaticity and feed-down sextupoles together with the beam-beam interactions. A systematic skew quadrupole component of a_1 = 1 unit in the arc dipoles[5] is included together with the skew quadrupole circuits that correct the minimum tune split to 0.001. Two different codes, MAD and Sixtrack, have been used for dynamic aperture tracking. The dynamic aperture (or chaotic boundary in the case of Sixtrack) typically agree to within 15%. Figure 2 shows a plot of the average dynamic aperture (after 10^6

[5] One unit of field gradient in the dipole represents a skew quadrupole field which value at 1 inch radius is equal to 10^{-4} of the dipole field.

turns or 2 seconds in the Tevatron) as a function of the proton bunch intensity from these codes. The averaging is done over several initial angles of the particles in physical space. The one sided error bars represent the minimum dynamic aperture at each intensity. This plot has two predictions: (a) the dynamic aperture of antiprotons at 150 GeV is nearly independent of the proton intensities over this range, (b) the dynamic aperture is about $3\sigma_{\text{total}}$. Tracking results also show that the dynamic aperture with beam-beam interactions drops by about $3\sigma_{\text{total}}$ compared to the case without beam-beam interactions.total

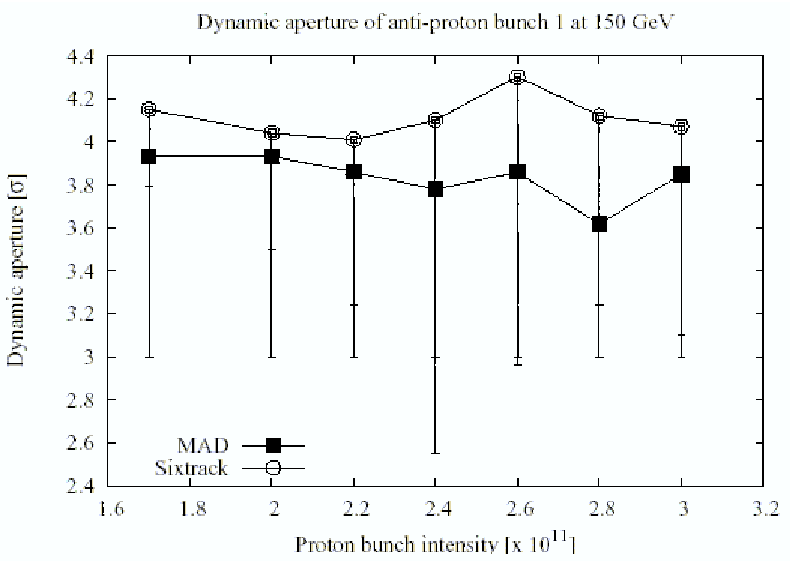

Figure 2. Dynamic aperture after 10^6 turns of antiproton bunch 1 vs proton intensity at injection with two different codes. The average value (over all angles in coordinate space) along with one-sided error bars to represent the minimum value at each intensity are shown; reference emittance is 15 mm mrad.

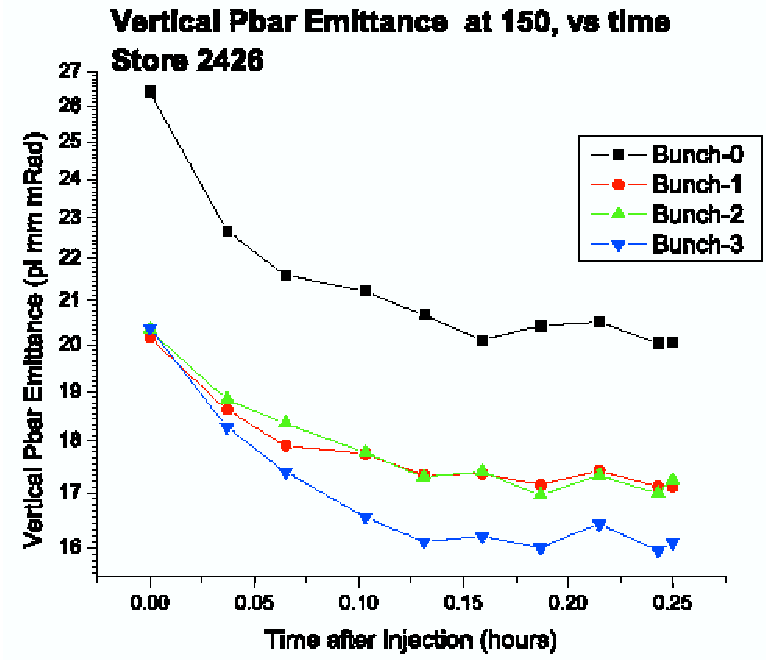

Figure 3. Evolution of antiproton vertical emittance with time at 150 GeV during a recent store.

Figure 3 shows the evolution of the vertical antiproton emittance of the first four bunches during a recent store. Because the initial emittance is larger than the equilibrium emittance for given dynamic aperture the diffusion and non-linear resonances cause the emittance decrease instead of its growth. The asymptotic emittance is therefore an experimental measure of the dynamic aperture. Using Eq. (3) we obtain that the vertical acceptance ranges from 30 to 38 mm mrad ($\varepsilon_{accept} = \varepsilon_{95\%} / (6 \cdot 0.09)$), which corresponds to 3.5- 3.9σ of 15 mm mrad emittance and is in a good agreement with data presented in Figure 2. Different bunches experience different long-range collisions and therefore have different emittances at the end of the injection. Because the beam consists of three trains of 12 bunches there is 3-fold periodicity in the antiproton bunch emittances. Figure 4 presents the typical beam emittances after beam acceleration and clearly demonstrates this periodicity. As one can see the emittance for bunches near abort gap experience smaller emittance growth. It can be reversed if tunes are changed.

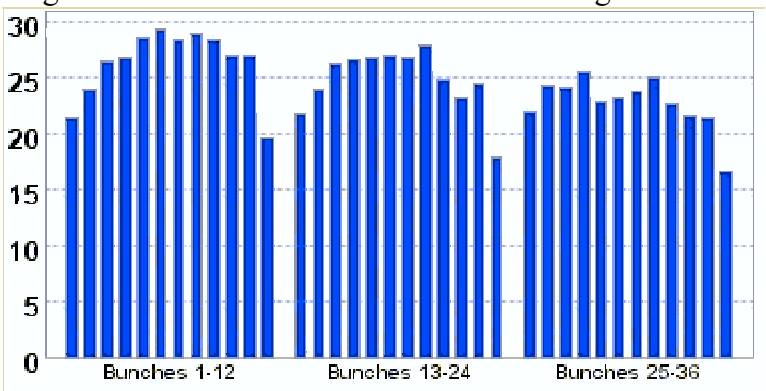

Figure 4. Antiproton horizontal beam emittances in mm mrad after beam acceleration measured by flying wires.

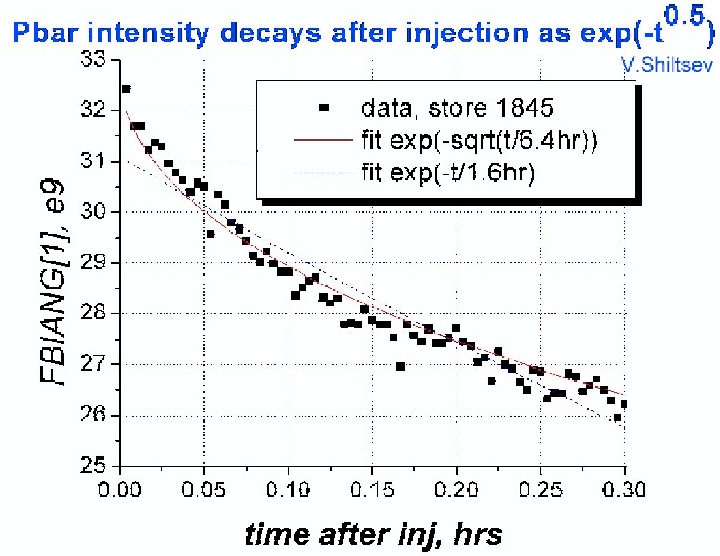

Figure 5. Dependence of intensity for antiproton bunch 1 on time after injection for Store 1845.

Figure 5 presents typical dependence of bunch intensity on time after injection. One can see that at the beginning the intensity decays very fast $\propto 1 - \sqrt{t/\tau}$, and then the decay slows down, and finally becomes exponential. The reason of such behavior is that the total extension of the initial beam distribution is larger than the dynamic or physical

aperture. This causes an immediate scraping of the tails of the distribution after injection, and creates a sharp fall to zero of the distribution function at the boundary value of the action variable. This "dip" propagates as a "diffusion wave" into the core of distribution proportionally to the square root of time after injection, $x \propto \sqrt{Dt}$, causing particle loss proportional to distribution function at the boundary, $\propto f(I_b)\sqrt{Dt}$. Similar behavior is also observed in the proton beam. There are tight aperture restrictions in all three degrees of freedom for both beams and we need additional studies to figure out partitioning of losses between the different planes.

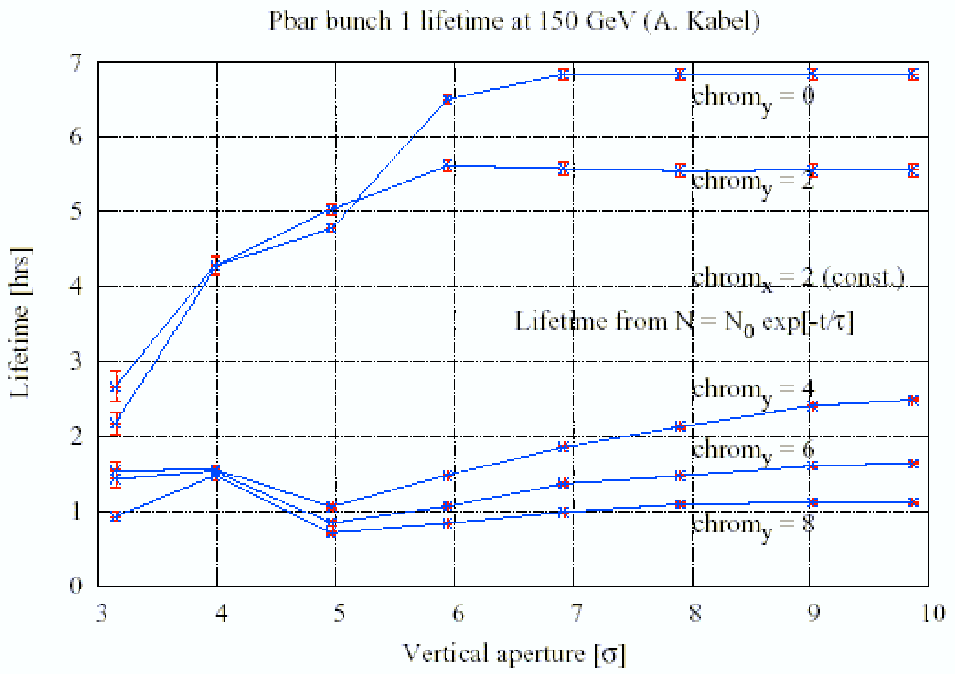

Figure 6. Lifetime of antiproton bunch 1 vs physical aperture at different vertical chromaticities in a simulation by A. Kabel (SLAC). Proton intensity per bunch = $2.2 \cdot 10^{11}$, the horizontal chromaticity is fixed at 2 units. There is a significant jump in lifetime when the vertical chromaticity is lowered from 4 to 2 units for all physical apertures greater than 4σ.

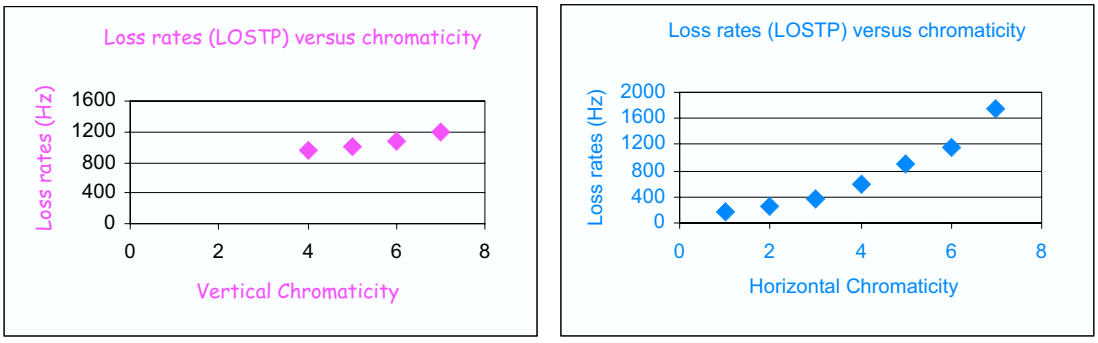

Figure 7. Dependence of proton loss on horizontal and vertical chromaticities.

Lifetime of both proton and antiproton beams is strongly affected by machine chromaticities. Figure 6 presents preliminary results of particle tracking performed by A. Kabel at SLAC for antiprotons. He has developed a six-dimensional code called PlibB. The features of this code include a fast algorithm for evaluating the beam-beam kicks and

a method for keeping track of the maximum amplitudes of each particle. This last feature allows a lifetime evaluation for any specified physical aperture after the end of the simulation. Transverse noise has been included to mimic the emittance growth from residual gas scattering. No other nonlinearities are included. Simulations at the NERSC facility, using ≈250 processors take ≈2 hours for a typical run (10^5 turns, $4 \cdot 10^5$ particles). The estimated statistical error is ±6.5% for a lifetime of 1 hour. The lifetime is shown as a function of the physical aperture for different settings of the vertical chromaticity. An interesting prediction is a significant jump in the lifetime when the vertical chromaticity is reduced below 4 units. A planned reduction of transverse impedance after the summer 2003 shutdown (see Section 6) should allow us to work with smaller chromaticities and is expected to improve antiproton lifetime. Figure 7 presents experimental data verifying strong effect of the beam chromaticities on the proton beam lifetime.

4.4.2. Ramp and squeeze

The RF voltage is kept constant in the course of beam injection and acceleration. Therefore the RF bucket size goes down by about 10% at the beginning of acceleration. Consequently, it causes a beam loss if initial longitudinal emittance is too large. Dedicated studies [17] have shown that the proton losses are determined by the longitudinal emittance and the quality of coalescing in the Main Injector. Long and/or poorly coalesced (i.e. non-Gaussian) bunches suffered the same or higher intensity loss as in regular stores while short nearly Gaussian bunches suffered losses less than 3%. Thus controlling the longitudinal emittance is important for limiting the proton losses. If correct tunes are kept in the course of acceleration the beam-beam effects on protons during the ramp do not appear to be significant at present antiproton intensities.

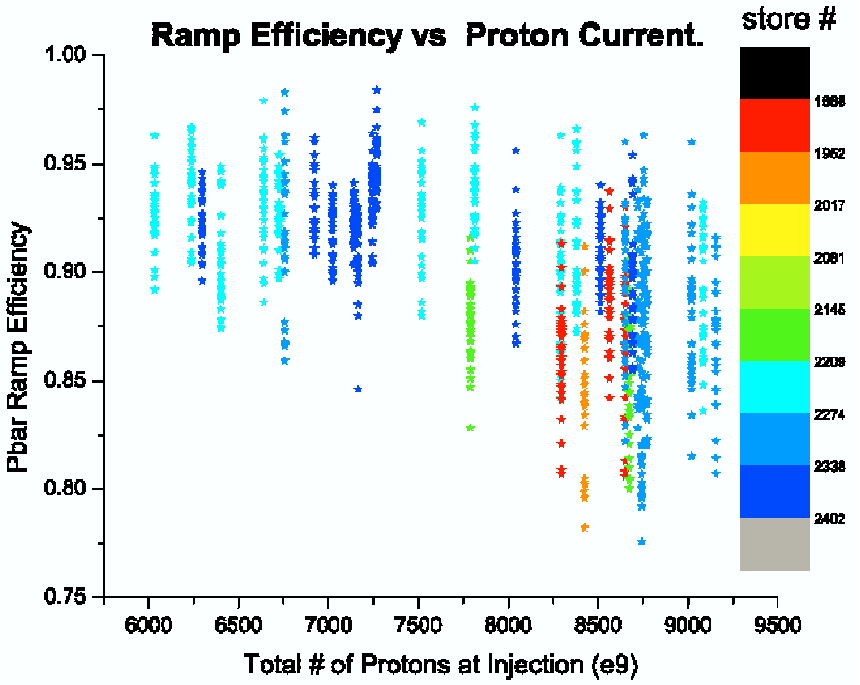

Figure 8. Antiproton ramp efficiency vs proton intensities in several recent stores (courtesy P. Lebrun).

Antiproton losses during the ramp were measured to be ~2% during a dedicated antiproton only store in September 2002. However during regular stores with protons present, antiproton losses averaged around 11% in March 2003. Figure 8 presents the

antiproton ramp efficiency as a function of the proton beam intensity. It clearly demonstrates that the beam-beam interactions cause higher loss at higher proton intensities.

The antiproton loss during the ramp is also well correlated with the antiproton vertical emittance, as seen in Figure 9. Reducing the emittance blow-up while injecting antiprotons in the Tevatron onto the antiproton helix would therefore also reduce the loss during the ramp. The longitudinal emittance of antiproton beam is smaller than for proton beam and therefore does not appear to have much influence on the antiproton losses during the ramp.

The strong effect of beam-beam interaction on the ramp efficiency is related with limited strength of electrostatic separators discussed in Section 3. At energies above 500 GeV there is not enough separator strength to maintain constant separations so the beam separations fall by about 30% during the second half of the ramp causing particle loss at the second part of the acceleration cycle.

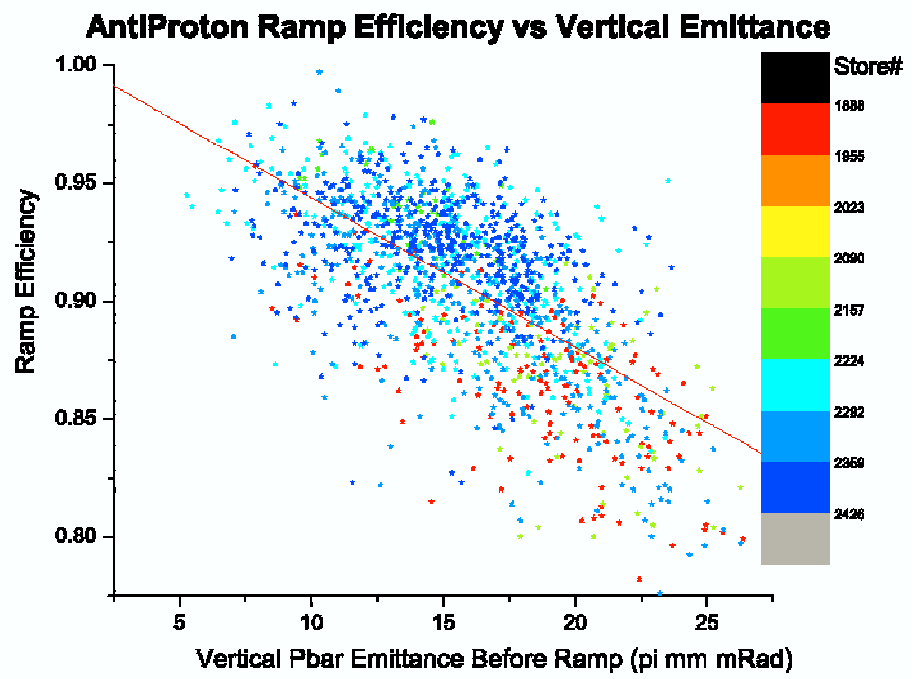

Figure 9. Antiproton ramp efficiency vs antiproton vertical emittance in several recent stores.

4.4.3. Collision

In several dedicated studies we have explored the possibility of improving the antiproton lifetime by changing the collision helix. In "the end of a store" study performed on March 21, 2003 the helix was changed in both planes simultaneously for the entire ring. The proton and antiproton losses as a function of the helix size are seen in Figure 10. Losses stayed nearly the same when the helix was opened by 20%. On decreasing the helix size, the losses in both beams decreased at first - perhaps due to the beams moving away from the collimators in the long arc or delayed response due to longer time to drift from the core to collimators. When the helix was reduced by more than 80%, losses climbed due to a combination of beam-beam effects and tunes changing with the helix size. Note that the study was performed at the end of store when the strength of the beam-beam effects is significantly reduced.

The experimental results from increasing the helix size at collision have been somewhat mixed so far. At higher beam intensities, it may nevertheless be advantageous to increase the beam separation so the development of possible methods to achieve this and experimental studies need to continue.

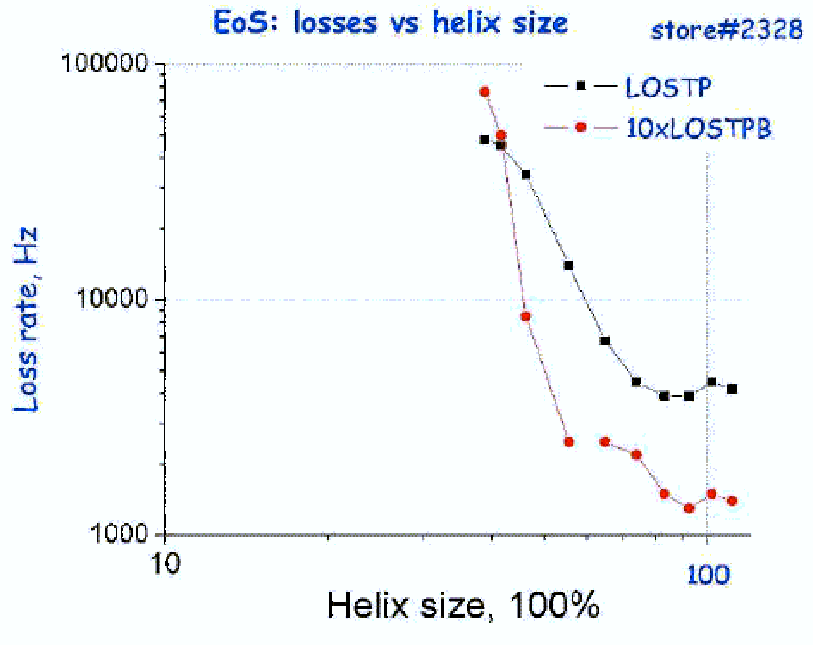

Figure 10. Losses as a function of the helix size observed at the end of a store (courtesy: X.L. Zhang)

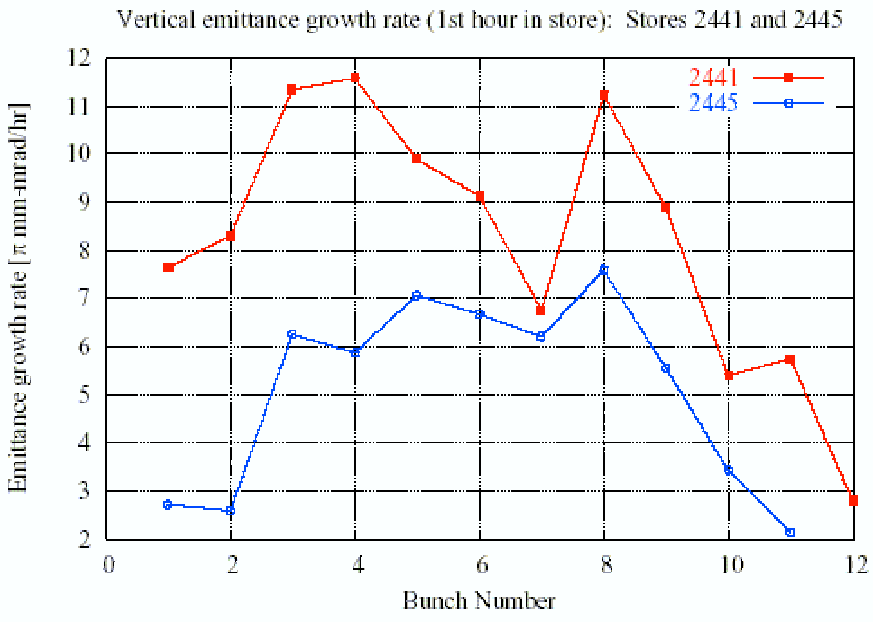

Figure 11. Bunch by bunch vertical emittance growth rates at the beginning of two recent stores. Lowering the vertical tune by 0.001 helped to lower the growth rate in Store 2445.

Emittance growth at the start of a store has occasionally been a concern. In most of these cases the antiproton emittance growth rate was large at the start, then dropped with falling beam intensities. This emittance growth is strongly bunch dependent; typically

bunches 1 and 12 have lower growth rates than the others. Small changes to the tune usually suffice to lower the growth rate. Figure 11 shows an example from two recent stores. In Store 2441 the growth rate was large for most bunches. In Store 2445 the vertical tune was lowered by 0.001, and the growth rate came down significantly. Even with the lower growth rate there is a difference amongst bunches, which we attribute to the differences in bunch tunes.

References

[1] Y.Alexahin, FERMILAB-PUB-00-120-T (2000).
[2] Y.Alexahin, FERMILAB-TM-2148 (2001).
[3] T.Sen, FERMILAB-Pub-00/093-T (2000).
[4] B.Erdelyi, T.Sen, FERMILAB-TM-2171 (2002).
[5] L.Michelotti, "Intermediate Classical Dynamics with Applications to Beam Physics". J.Wiley, 1995.
[6] A.J.Lichtenberg, M.A.Lieberman, “Regular and Stochastic Motion”, Springer-Verlag, NY, 1983.
[7] W.Herr, J.Miles, *in*: Proc. EPAC'96, Sitges, pp.424-426 (1996).
[8] B.Erdelyi, T.Sen, unpublished.
[9] Y.Alexahin, “Beam-beam effects at injection”, http://www-bdnew.fnal.gov/beam-physics-studies/Notes/2002/bb_SBR_at_inj.pdf
[10] J.Marriner, “Antiproton Tune Measurements”, 1996. (unpublished)
[11] A.W.Chao, "Physics of Collective Beam Instabilities in High Ehergy Accelerators", J.Wiley, 1993., pp.235-240
[12] Y.Alexahin, CERN SL-96-064 AP (1996); Particle Accelerators, v.59, p.43 (1998).
[13] K.Yokoya *et al*. KEK Preprint 89-14 (1989); Particle Accelerators, v.27, p.181 (1990).
[14] Y.Alexahin, LHC Project Report 461 (2001); NIM, A480, P.253 (2002).
[15] A.Hoffman, *in*: Proc. LHC'99 Workshop, CERN-SL-99-039 AP, Geneva, 1999, p.56.
[16] Y.Alexahin, *in*: Proc. Workshop on Beam-Beam Effects in Circular Colliders, FERMILAB-Conf-01/390-T, Batavia, 2001, pp.117-120.
[17] R. Moore, F. Schmidt, T. Sen, V. Shiltsev, Proton losses during acceleration in the Tevatron, Beams Division Document 535 (March 2003)